SANDIA REPORT
SAND2014-18860
Unlimited Release
Printed October 2014

Statistics of particle time-temperature histories

John C. Hewson, David O. Lignell, Guangyuan Sun

Prepared by
Sandia National Laboratories
Albuquerque, New Mexico 87185 and Livermore, California 94550

Sandia National Laboratories is a multi-program laboratory managed and operated by Sandia Corporation, a wholly owned subsidiary of Lockheed Martin Corporation, for the U.S. Department of Energy's National Nuclear Security Administration under contract DE-AC04-94AL85000.

Issued by Sandia National Laboratories, operated for the United States Department of Energy by Sandia Corporation.

Available to DOE and DOE contractors from
U.S. Department of Energy
Office of Scientific and Technical Information
P.O. Box 62
Oak Ridge, TN 37831

Telephone: (865) 576-8401
Facsimile: (865) 576-5728
E-Mail: reports@adonis.osti.gov
Online ordering: http://www.osti.gov/bridge

Available to the public from
U.S. Department of Commerce
National Technical Information Service
5285 Port Royal Rd.
Springfield, VA 22161

Telephone: (800) 553-6847
Facsimile: (703) 605-6900
E-Mail: orders@ntis.fedworld.gov
Online order: http://www.ntis.gov/help/ordermethods.asp?loc=7-4-0#online

SAND2014-18860
Unlimited Release
Printed October 2014

Statistics of particle time-temperature histories

John C. Hewson
Sandia National Laboratories
P.O. Box 5800
Albuquerque, New Mexico 87185

David O. Lignell, Guangyuan Sun
Brigham Young University
Provo, Utah 84602

Abstract

Particles in non-isothermal turbulent flow are subject to a stochastic environment that produces a distribution of particle time-temperature histories. This distribution is a function of the dispersion of the non-isothermal (continuous) gas phase and the distribution of particles relative to that gas phase. In this work we extend the one-dimensional turbulence (ODT) model to predict the joint dispersion of a dispersed particle phase and a continuous phase. The ODT model predicts the turbulent evolution of continuous scalar fields with a model for the cascade of fluctuations to smaller scales (the 'triplet map') at a rate that is a function of the fully resolved one-dimensional velocity field. Stochastic triplet maps also drive Lagrangian particle dispersion with finite Stokes numbers including inertial and eddy trajectory-crossing effects included. Two distinct approaches to this coupling between triplet maps and particle dispersion are developed and implemented along with a hybrid approach. An 'instantaneous' particle displacement model matches the tracer particle limit and provides an accurate description of particle dispersion. A 'continuous' particle displacement model translates triplet maps into a continuous velocity field to which particles respond. Particles can alter the turbulence, and modifications to the stochastic rate expression are developed for two-way coupling between particles and the continuous phase. Each aspect of model development is evaluated in canonical flows (homogeneous turbulence, free-shear flows and wall-bounded flows) for which quality measurements are available. ODT simulations of non-isothermal flows provide statistics for particle heating. These simulations show the significance of accurately predicting the joint statistics of particle and fluid dispersion. Inhomogeneous turbulence coupled with the influence of the mean flow fields on particles of varying properties alters particle dispersion. The joint particle-temperature dispersion leads to a distribution of temperature histories predicted by the ODT. Predictions are shown for the lower moments and the full distributions of the particle positions, particle-observed gas temperatures and particle temperatures. An analysis of the time scales affecting particle-temperature interactions covers Lagrangian integral time scales based on temperature autocorrelations, rates of temperature change associated with particle motion relative to the temperature field and rates of diffusional change of temperatures. These latter two time scales have not been investigated previously; they are shown to be strongly intermittent having peaked distributions with long tails. The logarithm of the absolute value of these time scales exhibits a distribution closer to normal.

Acknowledgements

This work is supported by the Defense Threat Reduction Agency (DTRA) under their Counter-Weapons of Mass Destruction Basic Research Program in the area of Chemical and Biological Agent Defeat under award number HDTRA1-11-4503I to Sandia National Laboratories. The authors would like to express their appreciation for the guidance provided by Dr. Suhithi Peiris to this project and to the Science to Defeat Weapons of Mass Destruction program.

Table of Contents

Introduction

One approach to neutralize biological agents involves the use of devices that provide either a thermal or chemical environment that is lethal to the biological agent. Such an environment is typically provided through an explosive dispersal process that is expected to cover much of the area of interest, but this blast can also displace agents in a manner that can reduce their exposure to the lethal environment. This project addresses the post-blast-phase mixing between the biological agents, the environment that is intended to neutralize them, and the ambient environment that dilutes it. In particular, this work addresses the mixing between the aerosols and high-temperature (or otherwise toxic) gases, and seeks to understand mixing environments that insure agent kill. Currently, turbulent mixing predictions by computational fluid dynamics (CFD) provide a certain degree of predictivity, and other programs are addressing research in this area. A significant challenge in standard CFD modeling is the accurate prediction of fine-scale fluid-aerosol interactions. Here we seek to study the statistics of particle interactions with high-temperature gases by employing a stochastic modeling approach that fully resolves the range of states (by resolving the full range of turbulent scales down to the molecular mixing scales). This stochastic approach is referred to as the one-dimensional turbulence (ODT) model and will provide a new understanding of low-probability events including the release of a small fraction of biological agents. These crucial low-probability events constitute the tails of a probability distribution function of agent release which are particularly difficult to model using existing approaches.

Of relevance to neutralizing biological agents is the fact that some time-integrated exposure is generally required. This work seeks to develop an understanding of time-integrated particle-environment interactions by quantifying the relationship between these histories and predictable quantities. Here, predictable quantities are those that can be predicted in the context of a CFD simulation that does not resolve fully the range of length and time scales and thus requires some modeling of the particle time-temperature histories. As will be discussed in the Statistics section below, this involves characterizing the relative motions of the particles and the high-temperature gases and relating these characteristics to predictable quantities. This will provide guidance on the modeling requirements for physics-based prediction of the particle time-temperature histories.

The primary method by which we will obtain statistics regarding the relative motions of the particles and the high-temperature gases is the ODT model [1-3]. In the ODT model, the full range of length scales is resolved on a one-dimensional domain that is evolved at the finest time scales. This allows a direct simulation of all diffusive and chemical processes along a notional line-of-sight through the turbulent flow. Turbulent advection is incorporated through stochastic eddy events imposed on the domain. The turbulent energy cascade arises in the Navier-Stokes equations through the nonlinear interaction of three-dimensional vorticity. This cascade results in length scale reduction and increased gradients. The ODT model incorporates these effects through "triplet maps," the size, rate, and location of which are determined by the state of a locally evolved instantaneous velocity field that provides a local measure of the rate of the turbulent cascade. The evolution of eddy events implemented through triplet maps reproduces key aspects of the turbulent cascade. That is, large scale fluctuations cascade to smaller scale fluctuations with increasing rate, while the magnitude of the fluctuations decreases appropriately, reproducing typical spectral scaling laws. In this work, we briefly review the physics of interest relevant to the application area. Then we summarize the implementation of Lagrangian particles into the ODT model. We discuss several comparisons between ODT predictions and experimental measurements that

serve to provide some confidence in the ability of ODT to predict quantities of interest. Finally, we provide some statistics of interest from simulations of non-isothermal free shear flows with Lagrangian particles to develop an understanding of particle time-temperature histories.

Before proceeding further, it is important to put the present ODT-based approach into the context of more traditional CFD simulation techniques. For Reynolds-averaged solutions of the Navier-Stokes equations, (RANS), only lower moments (e.g., averages) of quantities of interest are available and there is no information about the tails of the distribution, such as pockets of gas with low temperatures. For large-eddy simulation, LES, the finest scales are filtered; to the extent that these fine scales are important in determining the particle temperature history, LES needs to account for this in a manner that has to date not been examined. The present ODT modeling approach provides the information necessary to construct the required full distribution of states by explicitly resolving the fine-scale processes. At the same time, traditional CFD is better able to handle complicated geometric environments, in part because these methods are developed for those environments and in part because the simplifications employed in the ODT model are aimed directly at avoiding geometric complexity. In this sense, ODT is completely complementary to approaches like RANS and LES. RANS and LES have the greatest fidelity toward the large-scale dynamics while all of the small-scale processes are subsumed within models. Conversely, ODT prescribes a model for the large-scale dynamics, but completely resolves the small-scale processes including the statistically rare events. The link between these two complementary approaches is as follows. The driving force in ODT for the modeled large-scale mixing is the overall shear energy of the flow. This shear energy, in the form of an overall velocity gradient, gives a time scale for the turbulent cascade of large-scale fluctuations to the diffusive scales. Also input to an ODT simulation is a length scale and some information about boundary conditions. These quantities required for an ODT simulation tend to be well predicted by traditional CFD. Since the output from an ODT simulation includes information not accessible from traditional CFD, these approaches are nicely complementary.

Basics of particle time-temperature histories

It is known that biological agents can be neutralized through exposure to sufficiently high temperatures or chemically-hostile environments for a sufficient duration [4]. In this work we have focused on thermal inactivation as a model with the premise that net particle heating to some critical temperature, T_{cr}, is required to neutralize the particle. With this premise, to heat a particle to T_{cr} one should consider a simplified particle temperature equation

$$\frac{dT_p}{dt} = \frac{\left(T_g - T_p\right)}{\tau_h}, \tag{1}$$

where T_g and T_p are the gas and particle temperatures, respectively, and τ_h is the characteristic heating time for the particle. This heating time scale, τ_h, will depend on the particle size, its fractal nature, its thermal characteristics, the gas thermal characteristics and its slip velocity relative to the gas, among other things. In the present work, we take to τ_h be given except for the consideration of its slip velocity and, in particular, correlations between its slip velocity and the gas temperature field. A similar expression for exposure to a gas-phase chemical species, C_g, that has deleterious effects on the particle might be written

$$\frac{dC_p}{dt} = \frac{C_g}{\tau_c}, \tag{2}$$

where τ_c is the characteristic time for diffusion of C_g to the particle and C_p counts the accumulation to a lethal dosage. Since Eq. (2) is so similar to (1) the bulk of the discussion will refer to temperature evolution with the understanding that the discussion applies to both.

With Eq. (1) forming the basic particle evolution model at this stage, with $T_p > T_{cr}$ indicating a neutralized particle, an objective would be to determine the probability that the particle temperature exceeds the critical temperature, Prob($T_p > T_{cr}$). With this objective, in addition to the heating time scale, the important quantity that determines the particle temperature evolution is the gas temperature that a particle 'sees,' the environment temperature. There are two components to this observed gas temperature: the statistics of the observed gas temperature and the characteristic time scales of temperature extrema. To illustrate this, we discuss an environment temperature, T_g, that varies as a square wave between two values, one temperature below T_{cr} and one temperature above T_{cr}. During each segment of the square wave, the particle temperature exponentially approaches the environment temperature with a time constant τ_h

$$\frac{\left(T_{p,f} - T_g\right)}{\left(T_{p,0} - T_g\right)} = e\left(-\frac{\Delta t}{\tau_h}\right). \tag{3}$$

Here, $T_{p,f}$ and $T_{p,0}$ are the final and initial particle temperatures, respectively, for each wave segment of duration Δt. If τ_h is sufficiently small *and* if T_g is sufficiently large, then a single square wave might neutralize the particle. This is demonstrated in the upper panel of Figure 1. If this does not occur in a single square wave, then a sequence of multiple square waves might neutralize the particle *if* the duration between high temperature environments is smaller than the duration between low temperature environments as indicated in the middle and lower panes of Figure 1. Thus, to predict Prob($T_p > T_{cr}$) involves predicting the joint statistics of temperature and time scales. Of course, within a turbulent flow field the temperatures and time scales do not have a simple bimodal-delta-function distribution. These statistics are expressed in terms of the joint probability density function $P(T_g, \Delta t)$. This will be discussed in the following subsections after a comment regarding more complex particle neutralization criteria.

It is straightforward to employ nonlinear particle response models, and those nonlinearities will alter the statistical requirements associated with neutralization. For example, if variations in water vapor pressure are critical, these introduce a nonlinearity (vapor pressure being roughly Arrhenius in temperature) that could be tracked within the particle context. In this case, the particle neutralization criteria might instead be written Prob($p_{H2O}(T_p) > p_{cr}$) where $p_{H2O}(T_p)$ indicates the nonlinear relationship between the vapor pressure and particle temperature.

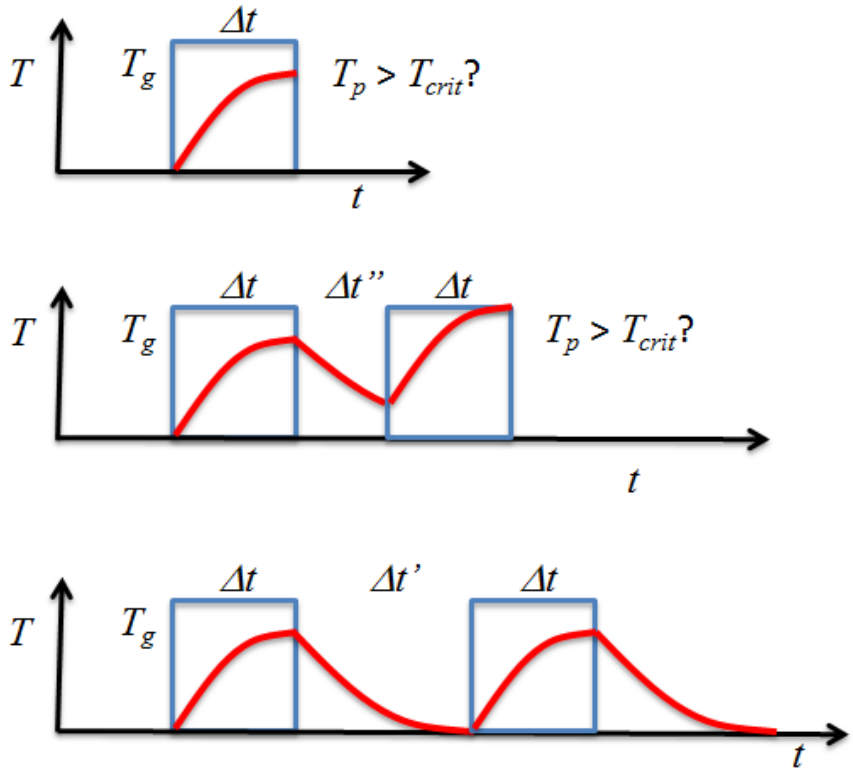

Figure 1. Particle temperature response to hypothetical gas-phase temperature following a square wave pattern with high temperature durations Δt and low temperature durations $\Delta t'$. Depending on T_g and Δt relative to T_{crit} and τ_η, the particle temperature may or may not exceed T_{crit}.

Statistics of gas temperatures

To leading order the temperature distribution is important. Generally in CFD the full distribution cannot be predicted without fully resolving the flow, so the distribution will need to be related to moments of the distribution: the mean temperature, its variance and the higher moments. The higher moments become more significant in identifying probabilities near the extremes of the temperature distribution. That is, near the edges of the turbulent flame when the typical temperature is not sufficiently high, we rely on intermittent excursions of high temperatures to neutralize particles. The probability of these intermittent high temperatures is described by the tails of the temperature PDF. Also important are the low temperature tails of the temperature distribution that might be associated with improbable failures to neutralize particles. In situations where mixing of hot and cool gases occurs in conjunction with heat losses, to walls for example, if the gas cooling occurs before mixing with cool gases containing particles, there might be a failure to neutralize particles. Higher moments affecting quantities such as skewness and kurtosis will also alter the relative durations of specific temperatures. This would alter the Δt associated with high and low temperature regions as in the square wave example.

Significant parameters determining temperature statistics include:

- Domain average temperature prior to heat losses, $T_{av,0}$, relative to T_{cr}.
- Magnitude of initial temperature fluctuations relative to $T_{av,0}$ - T_{cr}.
- Characteristic (wall) heat loss temperature, T_w, relative to T_{cr}.

- Time scale for mixing of hot gases with particle-containing gases relative to time scale for particle heating.
- Time scale for mixing of hot gases with particle-containing gases relative to time scale for heat losses.
- Time scale for mixing of hot gases with particle-containing gases relative to time scale for long-time heat release (fuel-oxidizer mixing or energetic particle burning).

It is important to note here that during the flow evolution, temperature inhomogeneities associated with unmixedness are dissipated, so that the time scale for mixing of hot gases with particle-containing gases is effectively a time scale for temperature homogenization. At the same time, the time scale for heat losses introduces inhomogeneities in the temperature field by introducing cool fluid elements. Depending on how distributed long-time heat release is this could introduce additional temperature inhomogeneities.

Figure 2 shows an example of a temperature PDF computed using ODT for a buoyant vertical wall fire. Ethylene fuel is fed through the wall at a rate of 390 L/min at 300 K. The PDF is shown at several distances from the wall at a height of 1.8 m. As the wall is approached the PDF peaks at higher temperatures. Away from the wall, the PDF peaks at lower temperatures due to air entrainment. The 0.15 m curve shows a bimodal distribution with a low-temperature spike at the air temperature. This would also occur very close to the wall (not shown) where peaks would occur at the cold fuel temperature and the hot flame temperature.

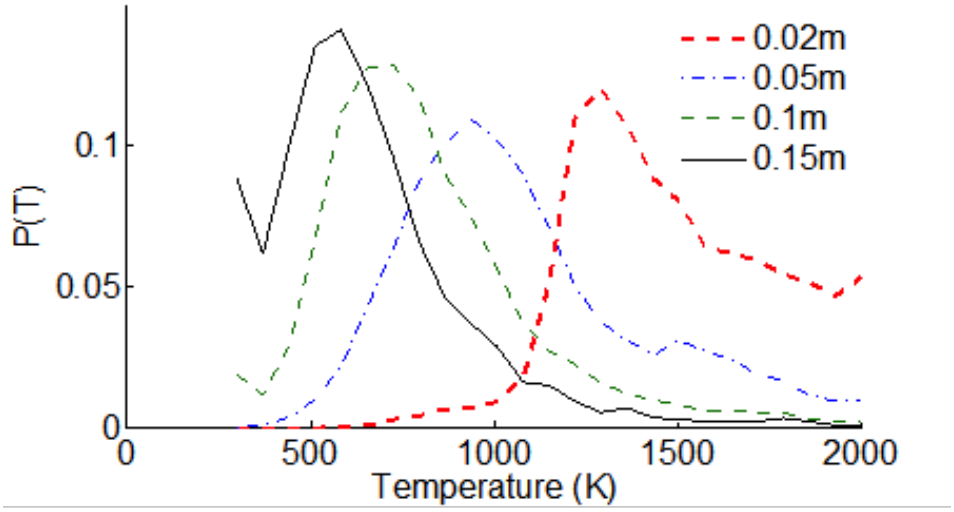

Figure 2. PDF of temperature at distances from a vertical wall fire at a height of 1.8 m computed using the present ODT code.

Relevant time scales for particle time-temperature histories

As discussed in the Basics of particle time-temperature histories section, the time during which a particle experiences a given temperature, relative to its characteristic thermal response time, is an important parameter. Time scales will exist for the evolution of the entire flow, and these integral time scales are readily determined using traditional CFD methods. These time scales for the overall flow evolution are expected to determine the typical particle response. However, individual particles will observe a range of temperature fluctuations about the mean behavior over varying time scales. A characteristic of turbulence

is that the time scales vary over many orders of magnitudes, and an advantage of the stochastic approach employed here is that this captures this full range of scales. Specifically, we provide the time scales associated with the rates of evolution of the gas temperature, T_g, from a Lagrangian reference frame moving with a particle.

The rate of temperature change from the particle perspective is written as

$$\left.\frac{dT_g}{dt}\right|_p = \left(v_p - v_g\right)\cdot\nabla T_g + \frac{DT_g}{Dt}. \tag{4}$$

The first term on the right-hand side of Eq. (4) describes the change in the observed temperature as the particle moves relative to the gas-phase field. This is particularly relevant for large ballistic particles (large Stokes numbers) that can move rapidly through the gas-phase field. This term involves the temperature gradient that will need to be understood at dissipative scales. The second term is written in terms of the substantial derivative for a fluid element

$$\frac{DT_g}{Dt} = \frac{dT_g}{dt} + v_g\cdot\nabla T_g \tag{5}$$

and describes the change in the gas temperature of that fluid element. This term is particularly relevant for small particles (small Stokes numbers) that follow the gas-phase flow since the velocity difference, $v_p - v_g$, approaches zero for these particles. It is noted here that the temperature conservation equation can be used to replace the right-hand side of Eq. (5) with

$$\frac{DT_g}{Dt} = \nabla\cdot\left(D_T\nabla T_g\right) + \dot{q} \tag{6}$$

which shows that the second term of Eq. (4) also depends on diffusion and reaction processes that occur at diffusive scales ($\dot{q}$ is the heat release rate).

Both sets of terms in Eq. (4) involve statistics of temperature gradients, diffusive processes or source terms. In general it is difficult to determine reactive scalar gradients within the context of CFD, and in the present work we will focus on relating these to the statistics of conserved scalars, their gradients and dissipation. That is, when the temperature is a reacting scalar, it will be related to other conserved scalars. A standard method of doing this is to relate the reactive scalars to the so-called mixture fraction variable that describes the (elemental) fraction of the fluid that originated in the fuel stream. Conditional-moment closure [5] and flamelet methods [6] are based on these relationships. To leading order, temperature and other reacting-scalar quantities are a function of the mixture fraction so that computation of the mixture fraction is often sufficient for describing the temperature evolution. This dependence of temperature on the mixture fraction is continuous and piecewise linear in the fast chemistry limit.

In the conserved scalar context, the conserved scalar dissipation rate

$$\chi = 2D\left|\nabla\xi\right|^2 \tag{7}$$

is appropriate for describing gradients, such as the temperature gradient appearing in the first term in Eq. (4). In Eq. (7), D is the diffusion coefficient appropriate for the scalar and ξ is the conserved scalar

(mixture fraction). It should be noted that the units of the scalar gradient can be thought of as "crossings per path length," and in the context of ballistic particles moving relative to the fluid, the frequency of crossings corresponding to specific temperature values are the objective.

The ODT simulations provide statistics for the gradient of the mixture fraction or the temperature that appear in Eqs. (4) and (6). It is of interest to express these statistics in terms of the inverse time scale for temperature changes that appears on the right hand side of Eqs. (4) and (6). For example, the probability density function (PDF) for the inverse time scale can be expressed from the statistics for these time scales. For the first term on the right-hand side of Eq. (4), the rate at which the temperature changes due to the particle moving through a temperature field, this PDF would be

$$P\left(\left(\Delta t\right)^{-1}\right) = P\left(\left(v_p - v_g\right)\nabla T_g\right) \tag{8}$$

where $P(x)$ is the PDF for x. This PDF will tend to be more important when particles have large slip velocities, associated either with larger particles or greater acceleration. The analogous PDF for the time scale associated with the first term on the right-hand side of Eq. (6) would be

$$P\left(\left(\Delta t\right)^{-1}\right) = P\left(\nabla \cdot \left(D\nabla T_g\right)\right) \tag{9}$$

Examples of these PDFs will be given below where it will be seen that the rates of temperature change in turbulent flows varies over several orders of magnitude. In some cases, it will be useful to conditionally sample the increasing and decreasing temperature separately and then to measure the statistics of the logarithm of that quantity. The statistics of the logarithm tend to be better behaved for processes like those associated with turbulent time scales.

Particle models within the ODT model

Lagrangian particles were implemented in the ODT code for this project based on the work of Schmidt et al. [7], who used ODT to study particle deposition in non-reacting flows. We have extensively analyzed the characteristics of the ODT-particle model including a sensitivity analysis of the additional parameter that appears in the particle model [8]. Further, we have extended the ODT particle model capabilities in two ways, providing for alternative couplings between the fluid and particle evolution described as type-C (and the option for type-IC) compared to type-I interactions described in the following. Further, we have developed algorithms for two-way coupling between particles and the fluid allowing the particles to modulate the turbulence, as occurs for example in flows where the particle mass fraction is not small; the two-way coupling is described in the subsequent subsection.

Particle eddy interactions

Prior to describing the ODT particle models, we note that ODT consists of two concurrent processes: (1) evolution of unsteady diffusion-reaction equations for mass, momentum, energy, and scalar components (e.g. chemical species); and (2) stochastic eddy events implemented using the triplet map described above that occur instantaneously and model turbulent advection. Details of the present ODT code and its implementation are available in Lignell et al. [9]. The particle evolution during diffusive advancement is similar to other Lagrangian particle approaches in which we integrate the particle drag law, specifying particle velocity and position on the line. Particle transport during eddy events is somewhat more challenging. Eddy events in ODT occur instantaneously, but the transport effect on particles occurs due to drag over a period of time. We have implemented two methods of describing the particle eddy interaction, type-I and type-C, as well as a hybrid method referred to as type-IC.

Eddy events for all eddy types are characterized by a position, a size L_e and a time scale τ_e. This eddy time scale is related to the rate of eddy events by a parameter β_p that is an adjustable constant within the model. Like in other multiphase flow models, this constant can be determined through predictions of eddy dispersion in the presence of non-negligible particle settling velocities. The analogy for k-ε particle models is the constants relating k/ε to the eddy lifetime [10, 11]. During an ODT eddy event, each location in an eddy is mapped to a new location according to the triplet map definitions in ODT. This local displacement is denoted Δx_e, and an eddy velocity is created as $v_e = \Delta x_e/\beta_p\tau_e$. This is the gas velocity felt by the particles during the eddy event. Each particle in the eddy region will interact with the eddy for a time $\tau_i \leq \beta_p\tau_e$. The interaction time will equal the eddy time if the particle remains in the eddy region for all of the eddy time. Otherwise, the interaction time is the time at which the particle trajectory takes it out of the eddy region.

The initial particle implementation, referred to as type-I (for instantaneous), gives an apparent instantaneous particle displacement related to the fluid displacement by the eddy, Δx_e, by the particle drag law assumed to occur over an eddy-interaction time. This eddy-interaction time occurs in parallel to the normal time evolution. This type-I interaction has several important features including rigorous matching of the tracer particle (or small particle) limit where the particles remain associated with fluid elements. This is important in the prediction of particle temperature evolution where the fluid diffusional processes are the most important effect in the evolution of the particle-observed temperature as per Eq. (6). Other aspects of our implementation of the type-I eddy interaction are given in Ref. [8]. Figure 3 graphically illustrates the type-I particle-eddy interaction process.

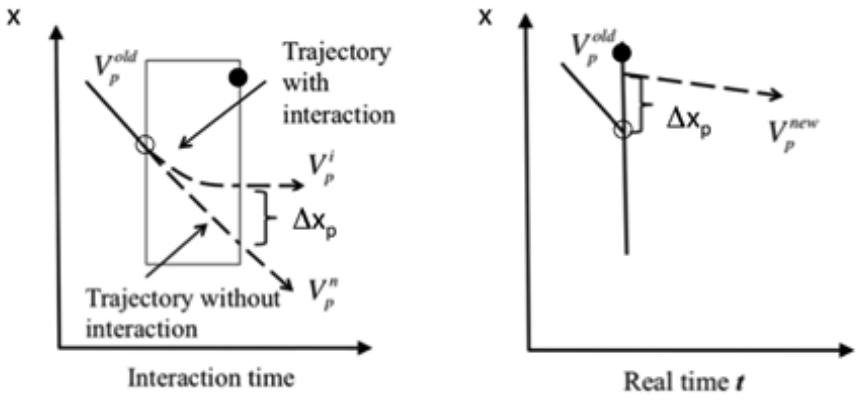

Figure 3. Particle trajectories during the type-I eddy interaction from Ref. [12]. In the eddy-interaction time frame the effect of fluid motion on the particle motion is determined (left). In the real time coordinate the particle displacement and momentum change associated with the eddy event appears instantaneous, as does the fluid dispersion (right). Open and closed circles show the initial and final fluid locations, respectively. The box indicates the eddy region in space-time.

To determine particle velocities and time correlations needed for predicting statistics of interest [12] the effective particle velocity field leading to that displacement is mapped backwards in time. This is discussed in detail in our publication [8].

The type-C particle-eddy interaction model differs in that the particle-eddy interactions are not discrete events like the fluid remapping during an eddy event. Rather, they occur in a continuous manner over a finite time during the diffusive advancement within ODT. As in type-I interactions, an eddy event induces a fluid velocity, $v_e = \Delta x_e / \beta_p \tau_e$, that acts on the particle through the drag law over a period of time given by the smaller of the eddy lifetime or the time that the particle leaves the eddy region. These velocities are mapped forward in time so that they occur continuously in time during the diffusive advancement. Figure 4 illustrates particle trajectories and the eddy locations for this type-C interaction, and can be compared with Figure 3. The type-C interaction is advantageous for simulation of larger particles where there is significant slip velocity. These particles can cross temperature minima and maxima as they cross an eddy and this is retained in the type-C interaction. Refer, for example, to the first term on the right-hand side of Eq. (4). Also note that the particle heat transfer coefficient is implemented as a type-C interaction for both eddy types as described in Ref. [12]. Unlike the type-I interaction, type-C interactions do not reduce to the tracer limit as the particle size is reduced; this is a disadvantage of the type-C model.

The third type of eddy interaction that has been implemented is a hybrid interaction referred to as type-IC. This acts as a type-I eddy for particles that are in the same location as an eddy event during the actual eddy event, while it acts as a type-C interaction for particles that cross into the eddy domain during the eddy lifetime. In this sense, it may be possible to simultaneously capture the important small and large particle limits within a single model. As of this report, we do not have sufficient results to determine whether there is a difference in the particle time-temperature history for the different eddy interaction types.

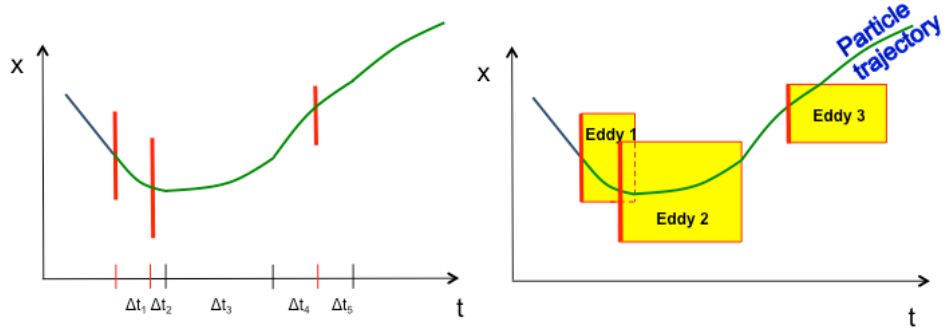

Figure 4. Illustration of notional particle trajectories in type-C interactions. The left plot shows the particle path and the eddy locations. The right plot shows the eddy interaction regions where it is seen that multiple interactions can occur simultaneously.

Comparison of type-I and type-C model attributes

In this section, the differences between type-I and type-C particle interaction implemented in this study are further disscussed. In a type-I interaction, the particle has an instantaneous *x* displacement when it is in an eddy region. That is, the particle goes through a discontinuous "jump" due to the eddy interaction, and then the interaction will expire immediately because the eddy event implementation is instantaneous. It turns out that each particle can interact with only one eddy during every type-I interaction. In contrast to type-I interactions, there is no instantaneous "jump" of particle motion in the type-C interaction; however there is a "jump" in the fluid properties associated with the triplet map. Although an eddy event is still instantaneous, the eddy effect on particles is allowed to exist in an interation time coordinate for the eddy duration. The particle has continuous interactions with eddies no mater when and where it enters the same space and time region as the eddy has. It is quite likely that one particle can feel the effects from multiple eddies simultaneously. Implementation of type-C interactions in ODT requires keeping track of the positions of all eddies from the time each eddy is born until that individual eddy's duration has expired.

In the type-I eddy model, the particles are less likely to interact with the eddy event when the line velocity becomes large. A particle only interacts with an eddy if it is in the eddy region when the eddy occurs, and this becomes unlikely if the particle traverses the domain quickly. In the limit of infinite particle velocity, the particle would not interact with any eddies since the particle trajectory and triplet maps would be paraellel lines. However, no matter what the context of the eddy interaction is, the type-C eddy model always allows the particles to interact with eddies when they occupy the same spatial-temporal coordinate.

In the type-C interaction, the particles are able to interact with the eddy in several different ways: (1) a particle could enter the eddy box in the line direction at the time the eddy is born (as in type-I); (2) a particle could enter the eddy box through the offline edges; (3) if the eddy is still active, a particle could re-enter the eddy through any edge of the box. In the implementation of the type-C interaction, we have deveoloped a new scheme to allow the eddy box to move in x, y, and z directions similar to the type-I interaction. That is, the relative motion of a particle and an eddy box is recorded in all directions until either the particle crosses out of the box or the eddy expires. This is important for the type-C interaction to capture the crossing trajectory effect.

In the type-I interaction, the eddy box moves in the off-line directions using the local fluid velocity. Conversely, an average velocity is used for the type-C interaction. Schmidt used an average velocity for all simulations [7, 13]. While there is some appeal in using an eddy-average velocity in the type-I interaction, there are inconsistencies that arise in certain cases. These are most readily observed in the case of tracer particles. Particles that exist in fluid elements with velocities differing from the eddy-average velocity can cross out of the eddy even though they remain associated with fluid elements. This results in a shorter eddy interaction time and less dispersion than that of the actual fluid elements. Naturally, this breaks the coincidence of fluid and tracer particles in type-I interactions. This early crossing effect is severe for tracer particles when the eddy-average box velocity is used, leading to significantly reduced tracer dispersion. It is possible to alter model coefficients to recover the appropriate particle dispersion, but differences will remain between the fluid and tracer evolution, and we find that the dependence of the dispersion on the Stokes number (or particle Froude number) is not correct.

For type-C eddies, the particles do not match the tracer limit and the sensitivity to the local versus eddy-averaged velocity is less significant. Further, the application of the local velocity is more complicated for type-C eddies since it evolves in time. For these reasons, the simpler eddy-averaged velocity is implemented for type-C eddies.

Dispersion can be interpreted in two senses: Einstein described Brownian motion using the rate of instantaneous displacements, while Taylor expressed fluid dispersion as the cumulative effect of velocity fluctuations over correlation times. The type-I and type-C approaches to evolving particles can be viewed as implementing approaches of Einstein and Taylor, respectively. While both approaches are valid, the existence of velocity statistics and some advantages of the type-I model (matching the tracer limit described above) encourages the development of velocity statistics in the context of the type-I model. For type-C eddies, the triplet-map driven eddy advection is observed during the diffusive time evolution since eddy velocities are mapped onto the spatio-temporal eddy box. For type-I eddies, the triplet map advection is observed instantaneously from the diffusive time evolution perspective. In order to better interpret the ODT processes, statistics for velocity evolution that would have led to the given displacements are obtained by defining the particle velocity histories. These velocity histories are composed of the velocity observed during diffusive evolution and, added to this, the velocity that would have led to triplet map displacements. This velocity leading to the displacements is mapped backward over the eddy interaction time. This is discussed and applied in detail in Ref. [8].

Two-way particle-fluid coupling

When the particle loading represents a significant fraction of the fluid mass, the particle phase will influence the flow through the exchange of momentum between the phases. This interaction is referred to as two-way coupling, and a key feature of two-way coupling for small particles of interest here is the reduction in the turbulence intensity and turbulence spreading rates because the particles reduce the velocity fluctuations. We have developed models to account for the influence of particles on the turbulence within the ODT context. The momentum coupling between the fluid and particle phases is accounted for directly during the diffusive advancement of the flow. During turbulent advection, the primary effect is through the eddy rate expression. In general the eddy rate expression is obtained from a measure of the available kinetic energy over the length of an eddy. In two-way coupling, the rate is adjusted in accordance with the change in particle momentum that would be associated with an eddy. In brief, the rate expression is the square root of the available kinetic energy per eddy length squared. The expression for the available kinetic energy is written as an integral over the eddy domain

$$\Delta E_i = \frac{1}{2}\int \rho\left[\left(v_i' + c_i K + b_i J\right)^2 - v_i^2\right]$$

where v_i is the i-velocity component and the prime denotes its value after the triplet map. The term $c_i K$ is a function that is added to the velocity component with the role of exchanging kinetic energy between the three velocity components, analogous to the pressure-scrambling and related return-to-isotropy effects that are well known to occur within turbulent flow [2]. The term $b_i J$ is the term that enforces momentum conservation for the velocity component [3]. In two-way coupling, the coefficient b_i is set to conserve momentum between the phases, and it is directly proportional to the exchange of momentum between the fluid and particle phases during an eddy. If the fluid would lose momentum to the particles during an eddy event, this term can reduce the eddy rate, or equivalently reduce the probability that a given eddy will occur. A detailed explanation of the expression and associated results will be given elsewhere [14]. Brief results are presented below in the section on Turbulent dispersion in particle-laden jets.

Tabular properties for fast reacting flow calculations

For combined particle-flame simulations, the time required to simulate finite-rate chemistry becomes an issue. Since the objectives of the present work do not include analysis of finite-rate chemical kinetics, but rather use the chemistry as a heat source, we have elected to develop a tabulation algorithm to describe the steady flame state as a function of a reduced set of parameters: the relative mass fractions of fuel derive elements referred to as the mixture fraction calculations to eliminate the fast chemical time scales from the calculations. This allows calculations limited by diffusion rather than chemical time scales.

We have implemented a two-dimensional table lookup algorithm that takes flamelet profiles as a function of the mixture fraction and its dissipation rate and returns the full chemical state. The tabulation provides composition, temperature, density, mean molecular weight, heat capacity, and other thermodynamic and transport data used in the simulation. Figure 5 shows the temperature field versus the mixture fraction and log of the scalar dissipation rate. The ODT code transports the mixture fraction and the scalar dissipation rate is computed from the mixture fraction profile. These two quantities are then used to look up properties (such as temperature) in the table as needed.

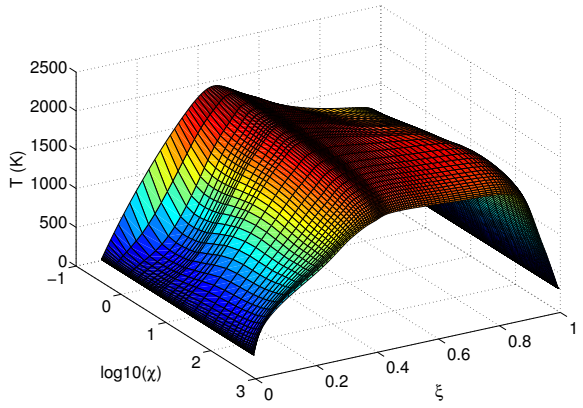

Figure 5. Flamelet table of temperature versus mixture fraction and scalar dissipation rate .

Particle Simulation Results in Isothermal Flows

Results of particle simulations are presented for four isothermal flows: (1) dispersion in homogeneous turbulence, (2) dispersion in dilute jets, (3) dispersion in jets with significant two-way coupling, (4) particle deposition in channel flows. These results serve to validate various aspects of the particle simulation model. In the next section the simulations are extended to several non-isothermal flows that provide sample results of relevance to determining particle time-temperature histories.

Turbulent dispersion in homogeneous turbulence

As relatively few studies have been performed of particle flows using ODT, the type-I particle model was validated for particle dispersion in decaying, homogeneous turbulence. Homogeneous turbulence is a well-studied flow configuration and allows us to focus on the particle model and dispersion physics. A paper was written as part of this project and has been accepted for publication in Physics of Fluids [8]. Here, a summary of the important results is presented.

We compare the ODT model to two classic experiments: those of Snyder and Lumley [15], and Wells and Stock [16]. These experiments generate turbulence by flowing air through a grid of bars. The turbulence intensity decays with time. Particles of varying sizes and densities are injected into the flow at a given point and the position measured. Statistics of many particles are gathered to determine the particle dispersion and other key properties. In the experiments of Snyder and Lumley (S&L), four particles were used: hollow glass (HG), corn pollen (CP), solid glass (SG) and copper (C). The experiment is run vertically, with particles accelerated by gravity. In the experiment of Wells and Stock (W&S) two particle sizes were measured, and an electric field applied to vary the body force on the particles. Both of these experiments used inertial particles with different Stokes numbers. A major objective was the investigation of the trajectory crossing effect, that occurs when particles are transported out of an eddy in a time less than the eddy lifetime. This generally occurs due to the body force accelerating particles, and results in reduced particle autocorrelation times and reduced particle dispersion.

The particle properties for the S&L case are summarized in Table 1, and for the W&S case in Table 2. Simulations were performed using 2048 ODT realizations. The ODT velocity was initialized using a sine wave with a wavelength equal to the turbulence grid spacing of 1 inch and an amplitude giving the same variance as a uniform profile (at U_0=6.55 m/s) that is blocked (u=0) at the bars making up the grid.

Table 1. Particle properties of Synder and Lumley [15].

Property	Hollow Glass	Corn Pollen	Solid Glass
Diameter (μm)	46.5	87	87
Density (kg/m^3)	260	1000	2500
$\tau_p f$ (ms)	1.7	23	58

Table 2. Particle properties of Wells and Stock [16].

Diameter (μm)	Density (kg/m^3)	$\tau_p f$ (ms)	Terminal velocity (cm/s)	Particle acceleration (m/s^2)
5	2475	0.192	5.86	305.2
"	"	"	17.06	888.5
"	"	"	20.91	1089.1
"	"	"	23.65	1231.8
57	2420	24.4	0	0
"	"	"	25.8	10.6
"	"	"	54.5	22.3
"	"	"	108	44.3

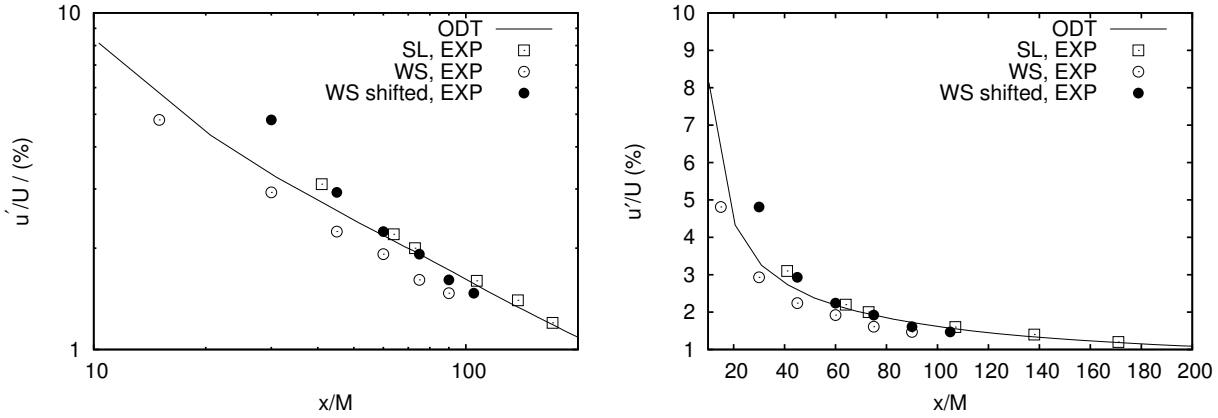

Figure 6. Homogeneous turbulenc decay rates on log (left) and linear (right) scales.

Figure 6 shows the ODT velocity decay compared to the experimental values of S&L and W&S. The ODT simulation is able to capture the expected power law decay rate. The figure shows results on a log and linear scales.

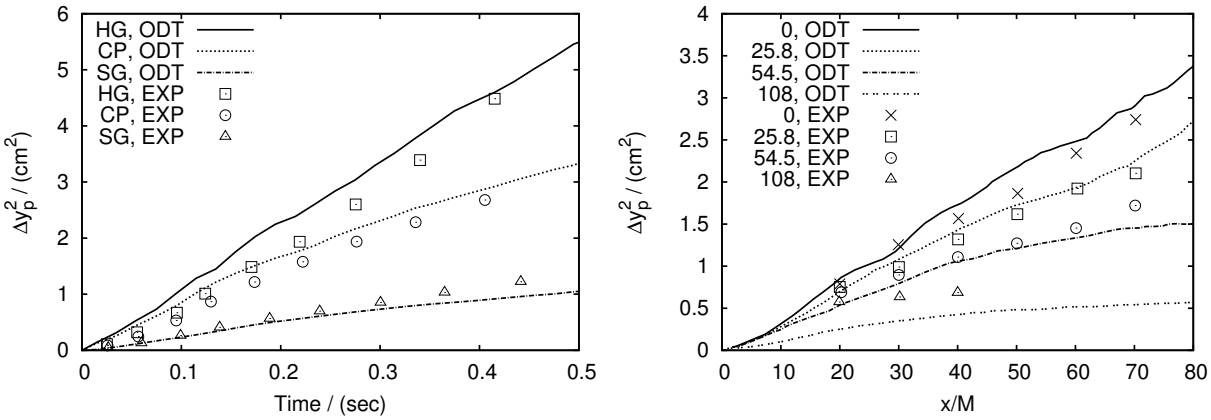

Figure 7. Particle dispersion for the S&L cases (left) and W&S cases (right).

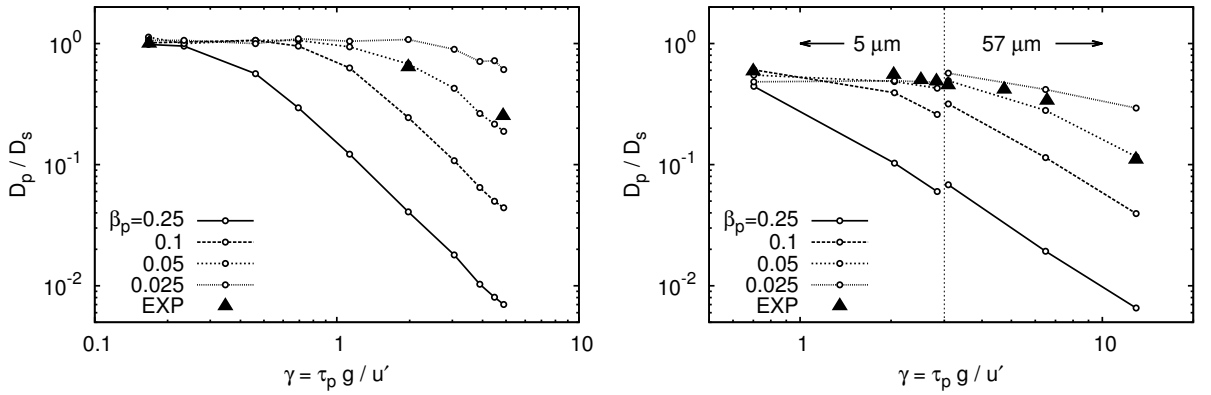

Figure 8. Normalized particle dispersion coefficient versus normalized particle terminal velocity.

The particle dispersion for the S&L and W&S cases is shown in Figure 7. The ODT particle parameter is β_p =0.05. The results show good agreement with the experimental data for the three S&L particle types modeled. As the particle timescale decreases, the dispersion increases, so that heavier particles are dispersed less than lighter particles. The hollow glass particles are light enough to behave nearly as fluid particles. The downward bend in the curves in Figure 7, with larger, heavier particles having a curve with a lower slope is a result of the trajectory crossing effect. Heavier particles have a higher terminal velocity under the influence of a body force. This results in these particles crossing more rapidly from one eddy to another, without the eddy imparting to the particle the full dispersive effect. With more rapid crossing the dispersion is reduced as shown in Figure 8.

The effect of the ODT particle parameter β_p on the dispersion results is illustrated in Figure 8. The figure shows the particle dispersion coefficient, normalized by the fluid particle dispersion coefficient, for various values of β_p. The dispersion coefficient is plotted versus the particle terminal velocity normalized by the fluid turbulent velocity u', denoted γ. At low values of γ, particles remain in an eddy for the duration of the eddy and the trajectory crossing effect does not occur. At higher values of γ, the terminal velocity is higher, resulting in trajectory crossing and reduced dispersion compared to the fluid particle dispersion. Higher values of β_p result in lower particle dispersion. The model compares best with the data when β_p=0.05, but it is clear that there is a strong sensitivity of particle dispersion to this parameter as it effectivly scales the particle-eddy interaction. The increased trajectory crossing with increasing β_p

and increasing τ_p is illustrated in Figure 9, which shows the fraction of particle eddy interactions that result in particles crossing out of eddies before the full eddy duration $\beta_p\tau_p$.

The particle dispersion coefficient may be written as $D_p = \Delta x^2_{PEI}/\Delta t_{PEI}$, where Δt_{PEI} is the time between eddy interactions, taken as τ_e, and Δx_{PEI} is the product of the particle eddy interaction (PEI) time and an eddy velocity: $\Delta x_{PEI}=\tau_i v_e$. In the trajectory crossing limit, the interaction time is the eddy size divided by the particle terminal veloity: $t_i=l/(2g\tau_p)$, and the eddy velocity is $v_e=\Delta x_e/\beta_p\tau_e$, where Δx_e is the triplet map displacement. Substituting these definitions into the expression for D_p gives

$$D_p = \left(\frac{l\Delta x_e}{2g\beta_p\tau_e\tau_p}\right)^2 \frac{1}{\tau_e}.$$

This gives $D_p \sim \tau_p^{-2}$ in the trajectory crossing limit, which is the same behavior observed in Figure 8 at large γ where the slope of the curve on the log-log scale is -2.

Other properties including the particle integral timescale, and particle turbulent kinetic energy were studied, as well as their dependence on the particle parameter β_p. In general, the ODT model is able to capture detailed particle dispersion statistics in turbulent flows. This validation study lends confidence to the model as more complex flow configurations are studied, such as jets, wall-bounded flows, and reacting flows.

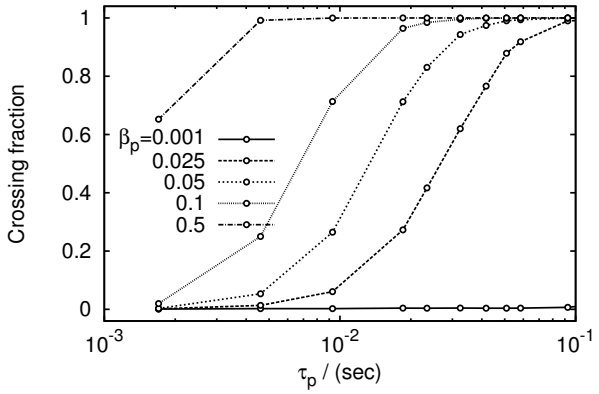

Figure 9. Fraction of particle eddy interactions that result in particles crossing out of an eddy before the eddy duration $\beta_p\tau_p$.

Turbulent dispersion in dilute jets

In most flows the turbulence is inhomogeneous, as occurs in jet flows, for example. In this section we compare dispersion over a range of particle and fluid time scales with measurements of Ref. [17]. Two nozzle diameters and three different gas exit velocities provide a range of fluid time scales. Two different particle diameters provide a simultaneous range of particle time scales resulting in a broad range of Stokes numbers. Figure 10 shows particle dispersion compared with measurements over the range of Stokes numbers and Reynolds numbers, while Figure 11 shows the particle velocities.

The jet configuration provides another good venue for indicating the sensitivity of the predictions to the value of the parameter β_p. In Figure 12 the dispersion for two of the cases can be compared for two different β_p values. This figure illustrates a general truth that the parameter β_p has a more significant

effect on particles with larger Stokes numbers. This is related to the larger slip velocity and the greater ability of particles with large slip velocities to cross eddies, reducing the eddy interaction time and thus the eddy dispersion. Slip velocities can also be important for impulsively accelerated flows as occurs with pressure waves. In general, the parameter β_p is not significant for very small particles that follow the fluid flow, that is for particles with Stokes numbers much less than unity. The dispersion of the smallest particles is more closely linked to the turbulent flow evolution.

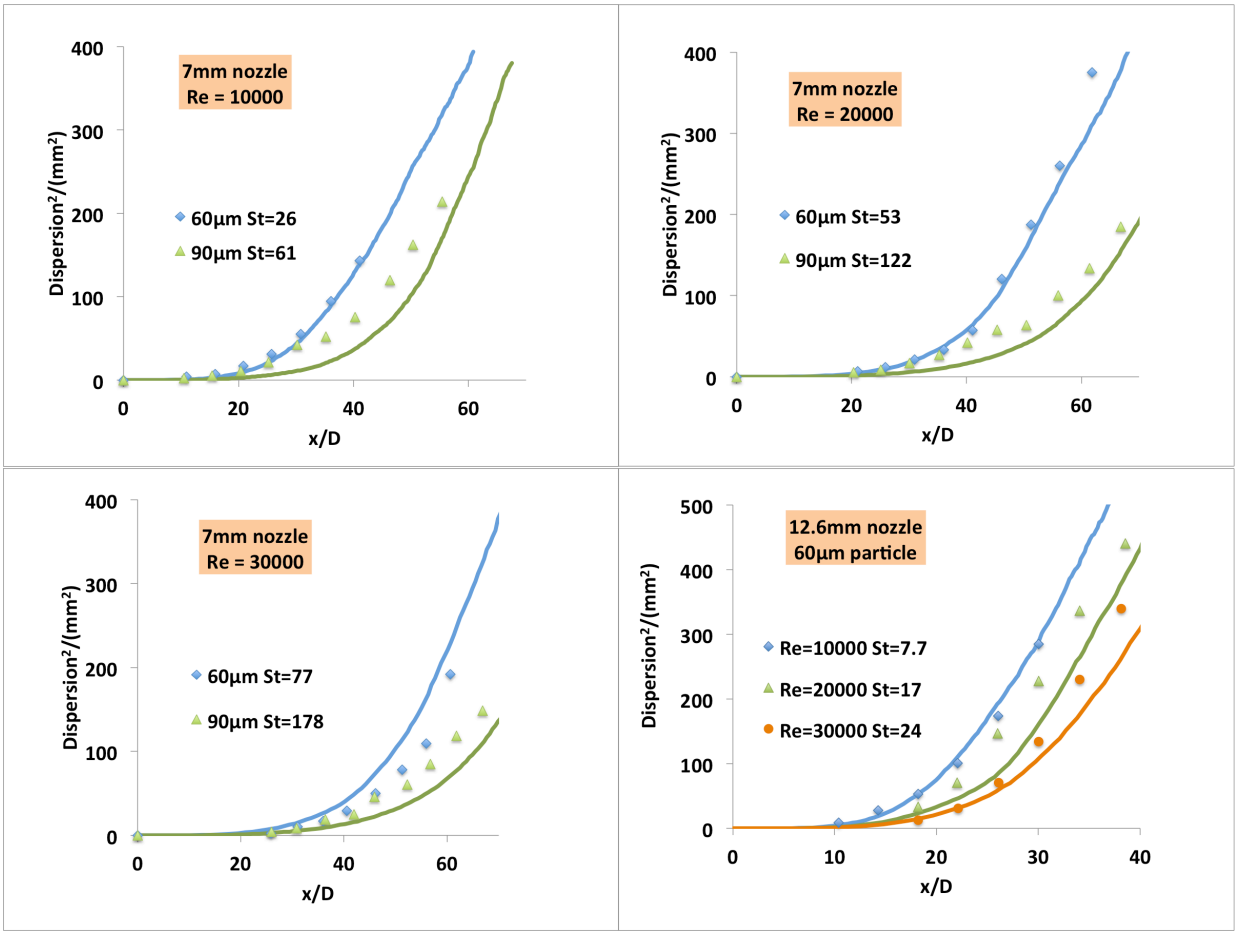

Figure 10: Predictions and measurements [17] of particle dispersion in dilute jet flows. Particle Stokes numbers and flow Reynolds numbers are indicated in each panel.

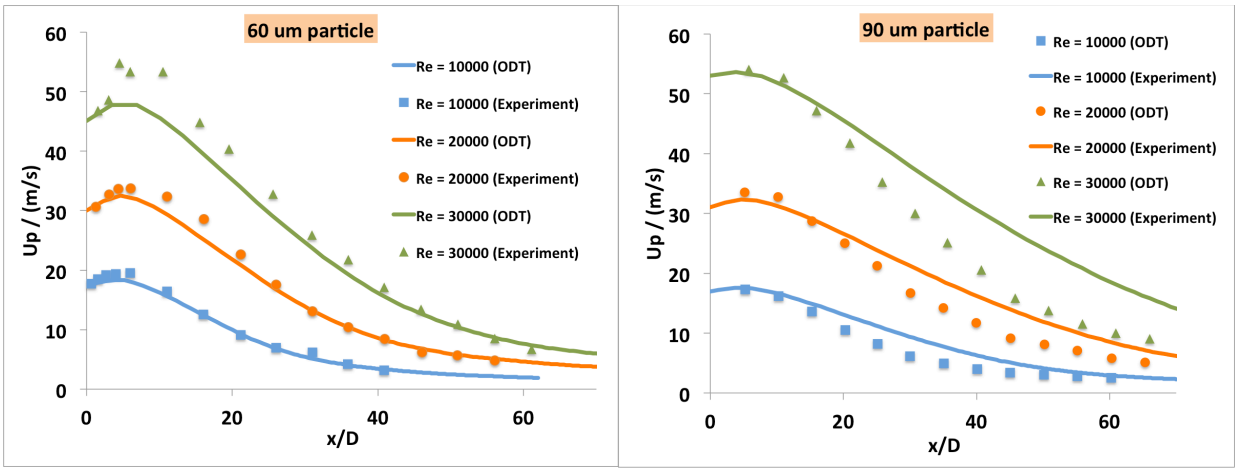

Figure 11: Predictions and measurements [17] of particle velocities in a dilute jet with a 7 mm nozzle.

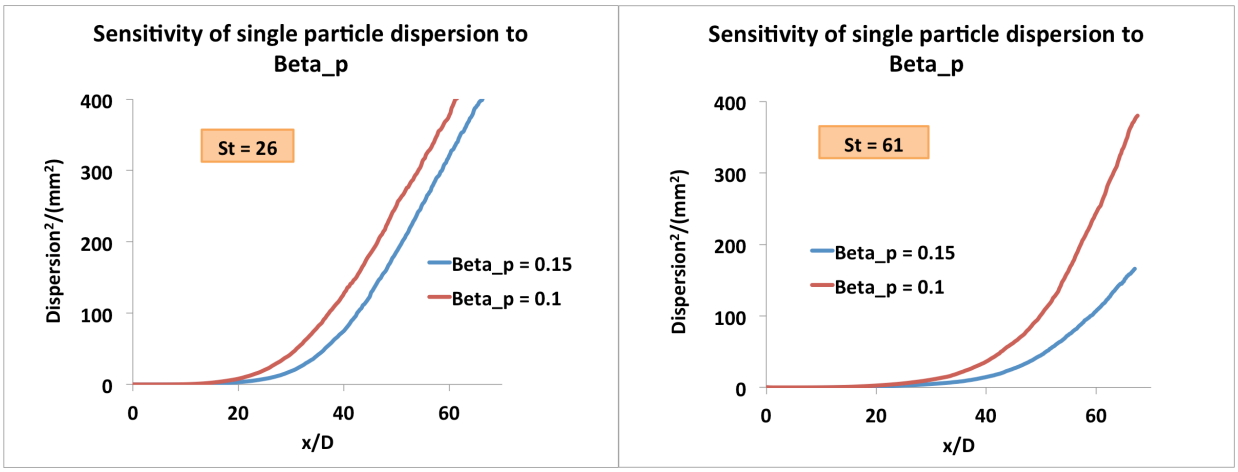

Figure 12: Dispersion predictions for two different values of β_p in dilute jet flows (7 m nozzle, Re = 10000) (c.f. Figure 10).

Turbulent dispersion in particle-laden jets

When particle loading is sufficiently large, the momentum transfer between the fluid and particle phase alters the flow and (for particles that are not large relative to turbulence scales) reduces the intensity of the velocity fluctuations. The two-way coupled flow capability is evaluated for flows where this is true. In this section we present what we will refer to as preliminary results since there are aspects of the model that are still under evaluation. The particle-laden jets as measured by Ref. [18] are used for comparison purposes here. These jets issue from a 1.42 cm nozzle at 11.7 m/s. We consider two different particle sizes (25 µm and 75 µm) having moderate Stokes numbers (3.6 and 10.8) and several different mass loading ratios (the relative mass flux of the fluid to the particle phase). In Figure 13, the fluid mean and fluctuating velocities are shown, and it is evident that the particle-laden jet mixes more gradually: the centerline velocity decays more gradually, and the turbulent fluctuations develop more gradually. Figure 14 and Figure 15 show the varying degree to which the flow is affected by different particle mass loading ratios and by different particle sizes.

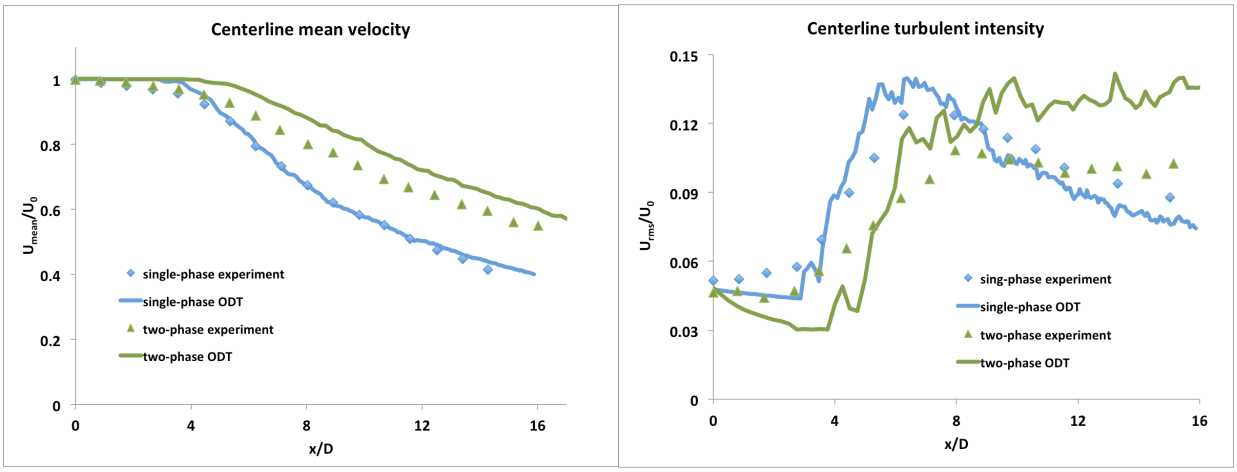

Figure 13: Comparison of predictions and measurements for flow without particles (labeled as the single-phase experiments) and the 50% solids loading with a particle Stokes number of 3.6.

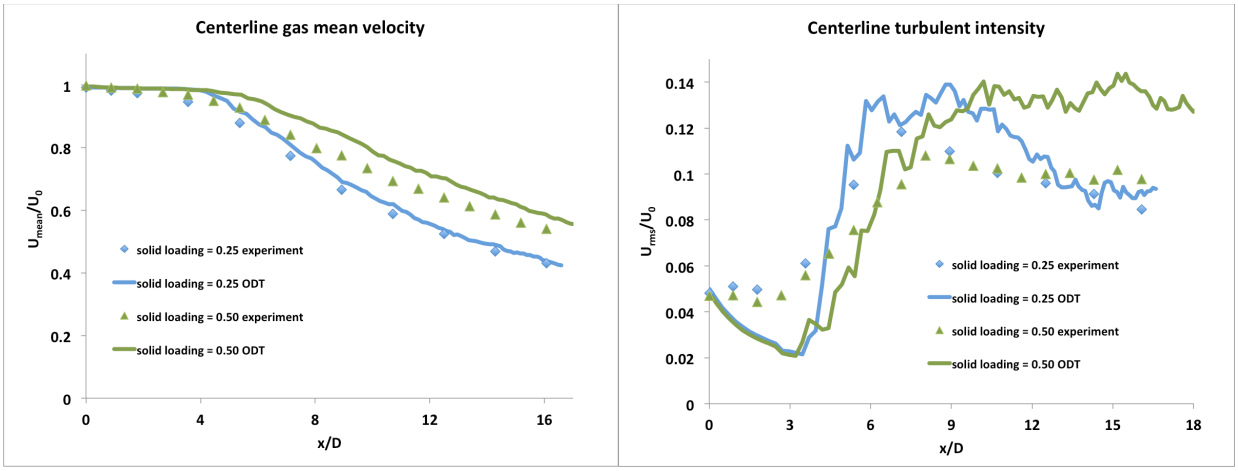

Figure 14: Comparison of predictions and measurements for flow with 25% and 50% solids loading with 25 µm particles.

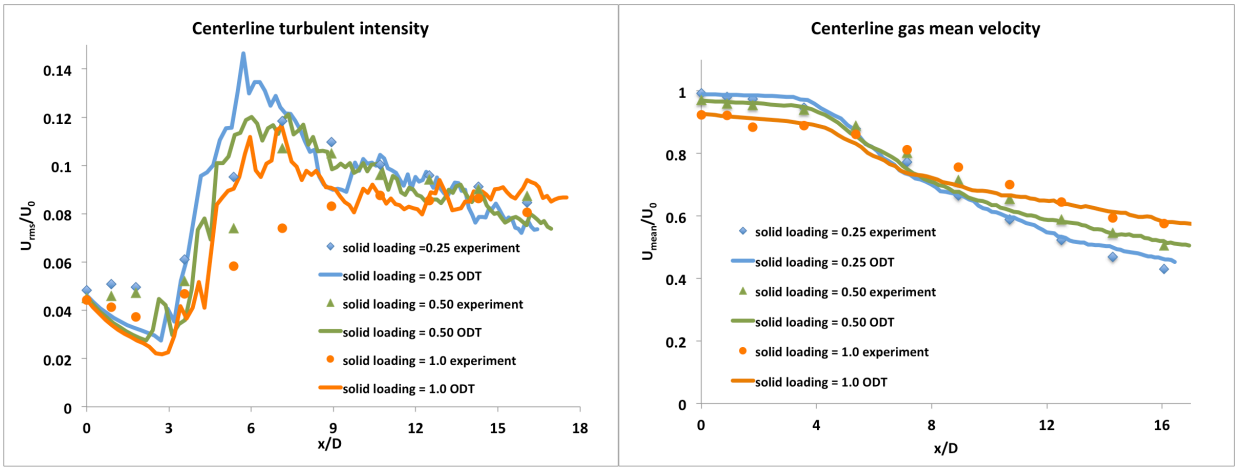

Figure 15: Comparison of predictions and measurements for flow with 25%, 50% and 100% solids loading with 75 µm particles.

Particle dispersion and deposition in channel flows

Another important configuration to study for particle-fluid interactions is channel flow. The inhomogeneities in turbulence fluctuations as the wall is approached lead to a net particle flux toward the walls that can be measured in an enhanced deposition process over certain parameter ranges. We have investigated the prediction of this deposition flux for the conditions described in Ref. [19]. The relevant parameter is the particle time scale normalized by the boundary layer friction time scale, referred to as τ_p^+. For particle deposition, three regimes are generally observed: For very small particle time scales, Brownian motion is the dominant deposition mechanism. This mechanism is not included within the ODT code at this point, although it can readily be included if required, and no predictions are made in this regime ($\tau_p^+ < 1$). For intermediate particle time scales, the deposition rate is a strong function of the particle time scale because inhomogeneous fluctuations tend to move particles toward the wall. This is the region that we have focused on to evaluate the ODT model's ability to handle inhomogeneous turbulence. Results for this regime are shown in Figure 16 for the conditions in Ref. [19]. For larger particle time scales, the particles are less affected by the turbulent fluctuations over the boundary layer and the deposition rate is reduced. Schmidt and Kerstein have argued using results of the ODT model that the observed fall off in the deposition rate may be even more significant in certain asymptotic limits that are difficult to measure [13].

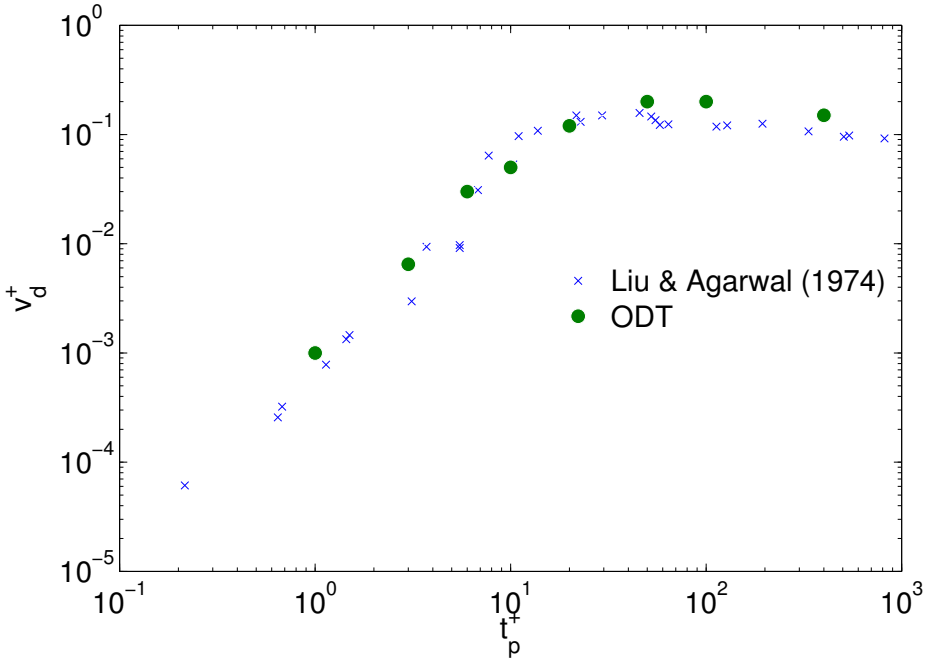

Figure 16: ODT predictions of wall deposition rates compared with measurements from Ref. [19].

Particle Simulation Results in Non-isothermal Flows

In this section we discuss particle time-temperature histories in non-isothermal flows. We focus on results for a high temperature jet interacting with particles of varying time scales that are initially outside the jet. The flow is bounded on one side by a wall. This particular configuration includes much relevant physics, but is not studied elsewhere (i.e. no measurements are available) so that validation is not possible. However, in none of these cases have we been able to find any measurements of particle heating. This points to the need for methods of studying these flows as provided by the current ODT particle models.

In carrying out non-isothermal flow simulations with the ODT model, it is important to note the continuity model applied in these simulations. The one-dimensional continuity equation is

$$\frac{\partial \rho}{\partial t} + \frac{\partial \rho u}{\partial x} = 0 \tag{10}$$

where u is here the velocity component along the ODT domain. Equation (10) requires any density changes associated with mixing to result in dilatational velocity changes [9]. For wall bounded flows, the wall boundary condition fixes the wall velocity so that dilatational velocities will tend to increase with increasing distance from the wall. In the present wall-bounded simulations this will be significant in the early mixing period where the fast initial mixing leads to rapid dilatation and velocity change. In free shear flows including the jet flows presented below the dilatation velocity is equally distributed, equivalent to matching pressure gradients on each end of the domain. In reacting jets, the dilatation is very strong and this dilatational velocity is also found to have an effect there.

Prior to addressing the simulation results, we discuss time scales. The results here can be generalized to some degree by appropriate normalization of the relevant time scales. Since there are no particular experiments to compare to, it is the ratio of time scales that is relevant here, for example the ratio of particle to flow time scales. Particle time scales have been selected based on heating time scale estimates that suggest single spore time scales are on the order of 10^{-4} s [4]. For small aggregates with on the order of ten particles, heat transfer to internal particles can be an order of magnitude slower [20-22]. In actual applications, it is likely that larger aggregates will exist with commensurately longer time scales. We have presented results here with particle time scales that vary from approximate time scales expected for single particles (3×10^{-5} s here) and up to three orders of magnitude larger. Fluid time scales have been selected so that single particles essentially follow the gas-phase flow while the largest particles significantly lag relative to the gas phase. Because the range of particle-to-flow time scales covers a wide range, it is possible to extend the results to other parameter regimes with suitable normalization.

A high-temperature jet interacting with surrounding particles

This subsection describes the configuration for a high temperature planar jet with significant kinetic energy (velocity) that then interacts with particles in a surrounding quiescent region. The basic configuration is depicted in Figure 17. On the left side of the domain the flow is bounded by a wall while on the right side of the domain the flow is open. Particles are located in the region between the high velocity, high temperature jet and the wall and also on the opposite side of the jet where the flow is unbounded. The initial particle locations are at y_0 = 0.02, 0.04, 0.06, 0.08, 0.27, 0.29, 0.31 and 0.33 m with the jet initial location extending from y = 0.1 to 0.25 m. To better denote their position relative to the jet, in the results the initial particle positions are expressed in terms of the jet radius with particles on

the wall side having negative initial position. In terms of $R_j = 0.075$ the initial particle positions are given below as $y_0 = -2.07R_j$, $-1.8R_j$, $-1.53R_j$, $-1.27R_j$, $+1.27R_j$, $+1.53R_j$, $+1.8R_j$ and $+2.07R_j$.

We note here that particles and fluid elements starting from a given location can disperse in either direction leading potentially to converging or non-converging paths (denoted as wavy lines in Figure 25). That is, a particle moved by dispersion closer to the high temperature jet would be expected to experience more interactions with high temperature gases while a particle starting from the same location could instead be dispersed away from the high temperature jet so that it experiences fewer interactions with high temperature gases. This can be expressed in terms of sequential conditional probabilities. We denote the conditional probability density function (CPDF) for the later position of particles originating at y_0 as $P(y \mid y_0)$ and the CPDF for the gas temperature observed by that particle as $P(T_g \mid y_0)$. These are related by the gas temperature CPDF $P(T_g \mid y)$ through the relation $P(T_g \mid y_0) = P(T_g \mid y)\, P(y \mid y_0)$. Statistics for each of these quantities are available from the ODT simulations.

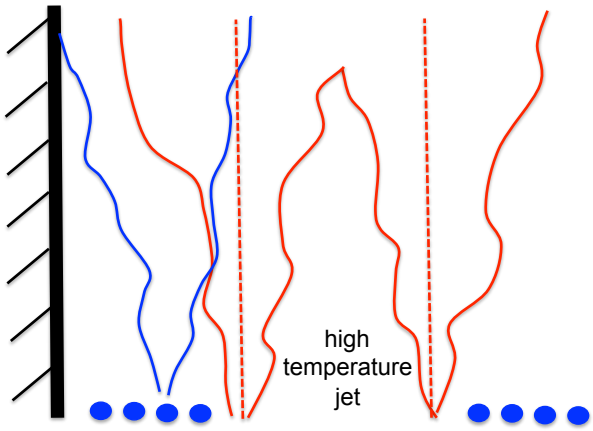

Figure 17. Schematic of hot jet configuration showing from left to right, (black) wall, (blue) array of four particle initial locations and hypothetical particle paths moving either toward wall or hot jet, (red) hot jet initial location (dashed) and dispersion of fluid elements both toward jet center and away from jet center, (blue) another array of four particle initial locations.

The jet Reynolds number based on the initial velocity and thickness is 225000, and the flow time scale based on the ratio of the velocity to the thickness is 5×10^{-4} s. The jet is taken to be the products of a stoichiometric ethylene flame, having an initial temperature of roughly 2300 K. We note here that the high temperature jet has a low density, so that mixing results in a narrowing of the jet in a mass-weighted sense that shows less dispersion in terms of temperature than a jet without the strong density variation; this is a consequence of the differences in the density between the jet and the surrounding ambient fluid. Also, this jet carries less momentum and kinetic energy per volume than a jet at ambient temperatures. In Figure 18 the average temperature field is depicted as it evolves over the duration of the simulation. The average temperature field is rapidly mixed in the early evolution when the time scales are shortest. The turbulence time scales start with the above noted 5×10^{-4} s based on the initial jet velocity and thickness and are expected to linearly increase in time after an initial transient so that for most of the duration shown here, the time scale is expected to be comparable to, though several times less than, the evolution time; results are presented below.

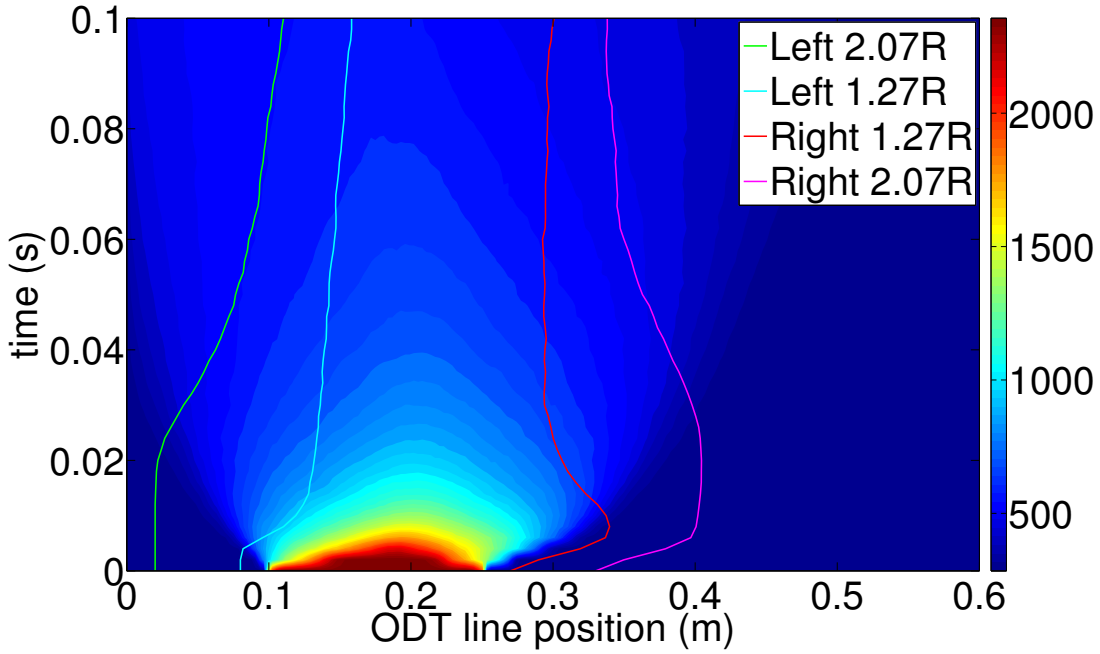

Figure 18. Temperature contour plot across the time-space domain covered by the ODT simulations presented in this section. The wall is at position 0 and the jet is initialized from 0.1 to 0.25 m.

Figure 18 also shows traces of the average particle position in time. Particle positions are discussed in detail below, but the trajectories here are a consequence of dilatation and inhomogeneous turbulence leading to inhomogeneous dispersion. The density difference described above will be significant in interpreting the results and is further discussed here. The hot jet is initially seven times less dense than the ambient air. While the hot jet initial width exceeds the thickness of the wall-side ambient region, the mass of air in the wall-side region is five times greater than the mass of air in the hot jet. As a consequence the mixing of the hot gases into the ambient air results in substantial and rapid cooling. Naturally, the unbounded ambient air on the far side plays a comparable role.

With four particles distributed on each side, we can estimate the degree of hot jet dilution that would occur before the gases containing the particles are entrained. A simplistic estimate is made by recognizing that the mass of air separating each particle and the jet is approximately equal to the mass of hot gases in the jet. That is, to a first approximation the hot jet would have been diluted twice (by equal amounts on either side to roughly one-third of the temperature difference) in order to mix with the nearest particles on the wall and far sides. The jet would have been diluted four, six and eight times in order to mix with the successive pairs of particles on each side of the jet. This simplistic analysis suggests that the jet maintains a square profile, that there are no turbulent fluctuations that disperse the particles and that there is symmetry between the wall and far sides. None of these conditions is satisfied, but the point to be noted is that the mass of air initially between each pair of particles is comparable to the mass of the hot jet and this provides an estimate of the degree of dilution to be expected. It will be seen that turbulence provides large fluctuations about this first estimate.

The flow interaction with particles is characterized by the evolution of time scales along with the evolution of the scalar (temperature) field shown in Figure 18. To further describe the flow field, the turbulent kinetic energy and its dissipation rate are computed from the ODT velocity field statistics. From

these values, estimates for the integral time scales and the turbulent diffusivity can be obtained and contour plots of these quantities appear in Figure 19. These provide a qualitative overview of the flow field evolution. The variation of the integral time scale across the domain with evolution time is shown in Figure 20. The integral time scale is initially much shorter as seen in Figure 19, but it increases, roughly linearly, as turbulent mixing occurs so that the relevant integral time scales for most of the evolution are a few times less than the evolution time. This is between the time scales for the two sets of larger particles with $\tau_p = \tau_h$ = 3e-3 s and $\tau_p = \tau_h$ = 3e-2 s. The spatial variation of the turbulent diffusivity across the domain is also shown in Figure 20 for different evolution times. The inhomogeneity in the turbulent diffusivity evident in Figure 20 will be significant in interpreting the results below. Fluid elements in regions of higher turbulent diffusivity will be more strongly dispersed and particle dispersion following the fluid elements should be similarly affected. There are two effects to note related to dispersion. First, during the development of the jet, there is a strong separation between the turbulent jet region with strong dispersion and the surrounding region with essentially no dispersion. Second, late in the evolution the turbulent region takes on characteristics of a boundary layer flow with increased dispersion farther from the wall associated with greater length scales; this latter phenomenon, while important to capture for fidelity, ends up not playing a significant role in the present results.

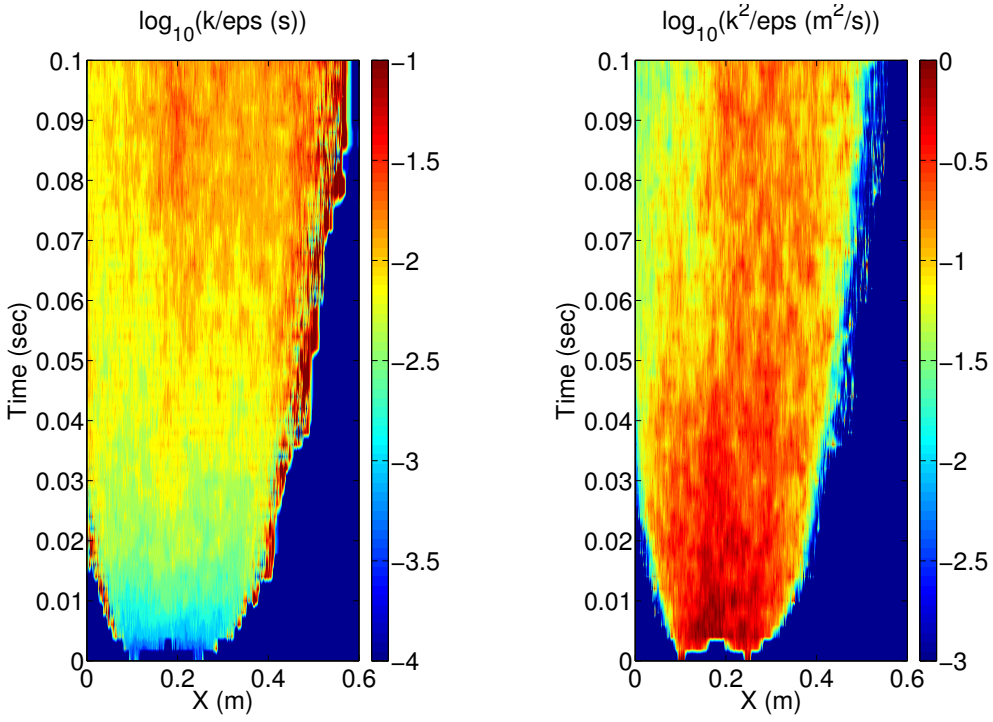

Figure 19. Contour plots for the integral time scale and turbulent diffusivity estimated from the turbulent kinetic energy and its dissipation rate.

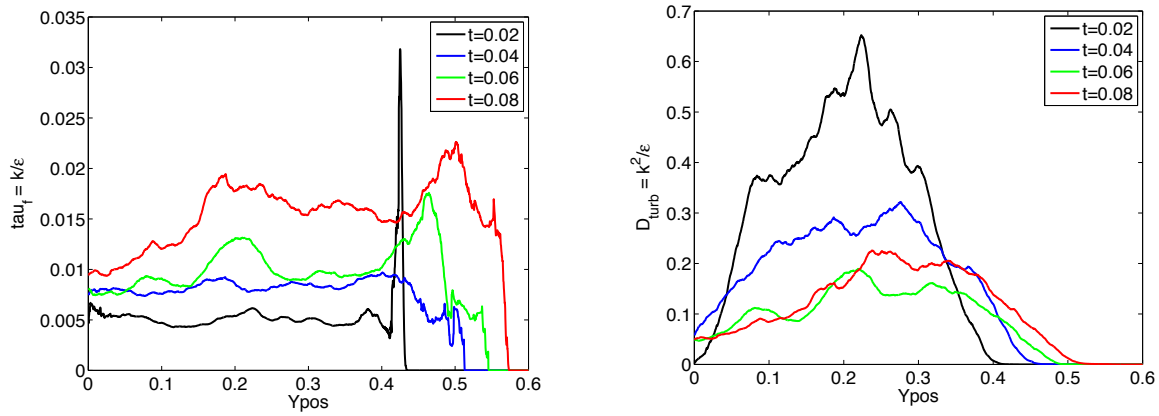

Figure 20. Turbulence characteristics at different times across the domain. The left panel shows the integral time scale estimated from the turbulent kinetic energy and its dissipation rate while the right panel shows the turbulent diffusivity estimated from the same quantities. Profiles are truncated in laminar regions to avoid division by zero.

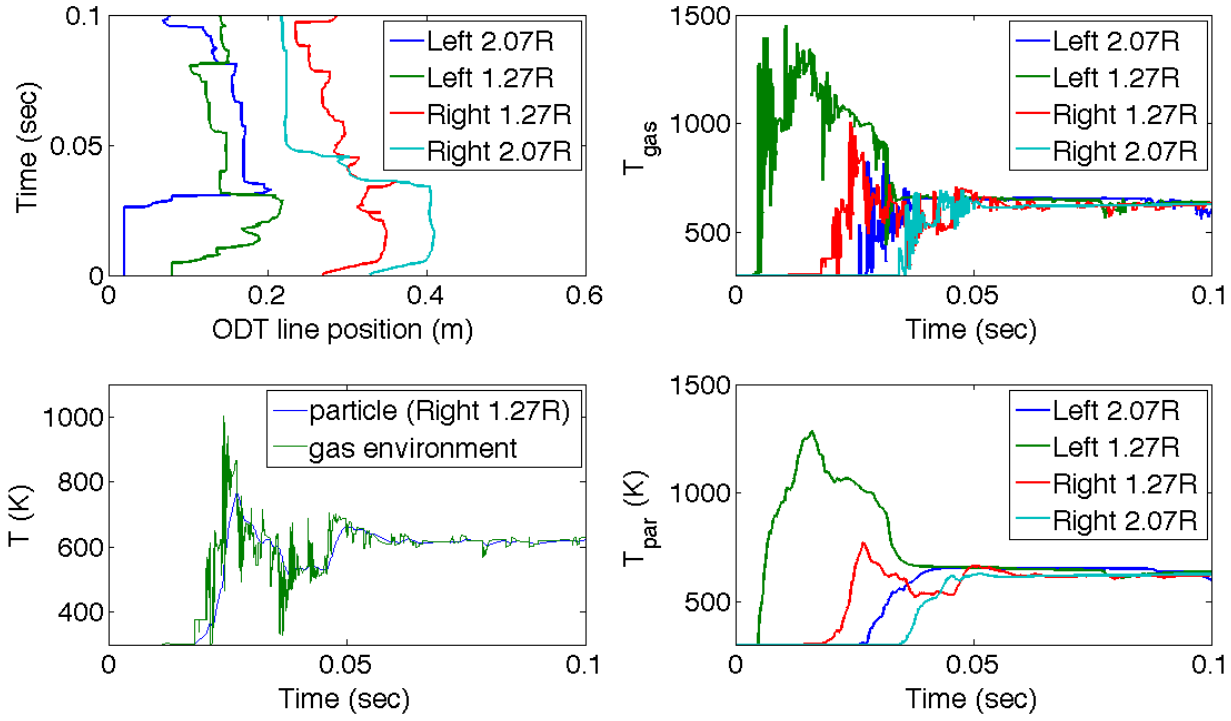

Figure 21. Instantaneous (single realization) profiles of particle evolution. Upper left, position of four particles versus time; upper right, gas temperture in the particle environment for four particles; lower right, particle temperature for four particles; lower left, gas and particle temperature for single particle.

In Figure 21 a series of instantaneous profiles from a single realization correspond to a particle with $\tau_p = \tau_h$ = 3e-3 s are presented for reference. Single realizations like this have limited meaning, but the ensemble of these simulations provides statistical properties of turbulent multiphase flow. The results show typical trajectories for several particles exhibiting intermittent motion characteristic of the ODT model. The gas temperature field observed by these particles and the particle temperature response to that field are also shown. The temperature results show how these particles act to filter high frequency

temperature fluctuations, and this is particularly clear in the lower left panel of Figure 21 where the gas and particle temperature for a single particle are overlaid. We note here that, while these particles appear to significantly filter the high frequency gas temperature fluctuations, the average and root mean square (rms) gas and particle temperature statistics look quite similar (c.f. Figure 26 and Figure 31).

Particle positions as a function of particle time scales and relative position

Particles are initially located outside the jet, either to the 'wall side' or to the 'far side.' This nomenclature will be employed in the discussion. As discussed above, four particles are evenly distributed on either side of the jet such that the spacing between the wall-side particles is even between the jet and the wall. The mass of air between each set of particles is comparable to the mass in the jet as is the mass of air between the nearest particles and the jet.

Figure 22 shows the average wall-side particle positions and their dispersion about the mean position. There is an initial delay before the jet interacts with the particles evident in both plots. After the jet interacts with particles, the particles are dispersed as expected with the particles nearest the high intensity mixing regions having higher dispersion rates. The intensity also varies across the mixing region so that the average position shows entrainment of particles into the jet. This is partially due to the dilatation of the flow as hot gases near the jet center are cooled and partly due to the inhomogeneous nature of the turbulence discussed below. The spatial inhomogeneities in the turbulence along the ODT domain are shown in Figure 20. These inhomogeneities in the turbulence lead to inhomogeneous particle dispersion. This inhomogeneous particle dispersion is clear in the particle position PDFs shown in Figure 23 where the PDF develops a long tail toward the center of the hot jet region where the turbulence is more intense. These PDFs are conditional position PDFs where the conditioning is on the original particle location and its time scales; this can be formally denoted as $P(y_{pos}|\, y_0, \tau_p, \tau_h)$. The particle PDFs for the wall-side particles also show the dispersion of some particles to the walls where they stick (as prescribed in the model). This dilatation and inhomogeneous turbulence leads to another unusual result that is the greater dispersion of larger particles. This greater dispersion of the larger particles is attributed to these particles being in regions of higher turbulence as indicated by their average positions in Figure 22.

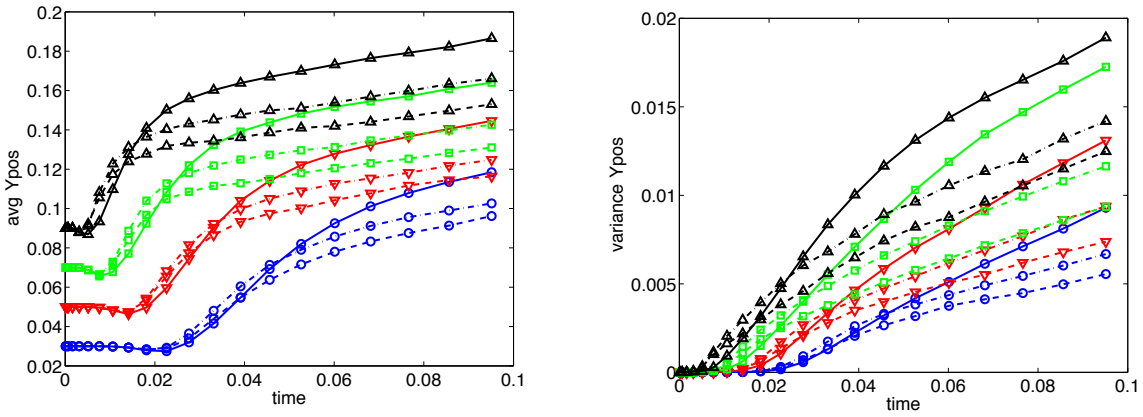

Figure 22. Average (left) and variance (right) particle positions for wall-side particles. From the wall to the jet, particle initial locations are denoted with blue circles ($y_0 = -2.07R_j$), red gradients ($y_0 = -1.8R_j$), green squares ($y_0 = -1.53R_j$) and black triangles ($y_0 = -1.27R_j$). Particle time scales are denoted by line pattern with solid denoting $\tau_p = \tau_h$ = 3e-2 s, dash-dot denoting $\tau_p = \tau_h$ = 3e-3 s and dashed denoting $\tau_p = \tau_h$ = 3e-5 s.

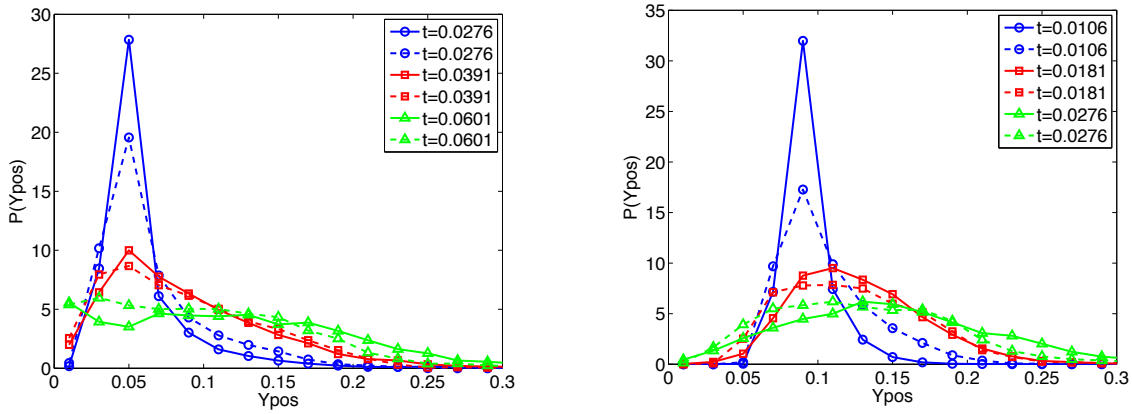

Figure 23. Particle position PDFs for particles with $y_0 = -1.8R_j$ (left panel) and $y_0 = -1.27R_j$ (right panel) at various evolution times. Small particles ($\tau_p = \tau_h$ = 3e-5 s) denoted with dashed lines while large particles ($\tau_p = \tau_h$ = 3e-2 s) denoted by solid lines. Note that times for different particles will differ because of the times at which the plume interacts with them.

Average positions and dispersion for the far-side particles are shown in Figure 24. Here the nature of dilatation in the ODT model, with the wall displacement being fixed and the dilatation increasing away from the wall, is evident as the initial average behavior is for particles to be pushed away by this dilation until the jet interacts with them. For the smaller particles (dashed and dash-dot lines in Figure 24) the particles largely follow the flow. Particles initially move outwards due to dilatation; as the turbulence interacts with these particles, the inhomogeneous nature of the turbulence (Figure 20) leads to more dispersion toward the jet center. This is particularly evident in the particle position PDFs shown in Figure 25 for the nearest and second nearest particles on the far side. In the PDFs an initially narrow distribution develops prominent tails toward the jet center with more gradual spreading of the distribution away from the jet center where the turbulent mixing is less intense.

The behavior of the large particles ($\tau_p = \tau_h$ = 3e-2 s) differs significantly from the smaller particles. In the earliest mixing period there is strong jet mixing leading to rapid dilatation evident in Figure 24. Initially these larger (heavier) particles lag behind the small particles and fluid elements. The turbulent mixing rapidly reaches the nearest particle to the jet; it is entrained first and is mixed well into the jet. The inertia from dilatation carries other larger particles mostly beyond the early turbulence and these particles are not entrained by the hot jet until late. This different behavior is evident in the solid lines describing these large particles in Figure 24. There the nearest large particles (black solid line) are entrained more and experience more dispersion than fluid elements because they lag behind the dilatational flow. The other farther largest particles (other solid lines) follow inertial trajectories beyond the fluid elements and do not undergo significant dispersion until later (Figure 24). Because these particles interact much less with the turbulence, we will focus less on those results. The particle PDFs for the larger particles are also shown in Figure 25. The nearest larger particles (left panel) mix more rapidly than the smaller particles because they exist within the higher intensity turbulence regions of the jet. The farther larger particles (right panel) have delayed mixing because of their position beyond the majority of the turbulent region with only a tail in the distribution developing late in the simulation.

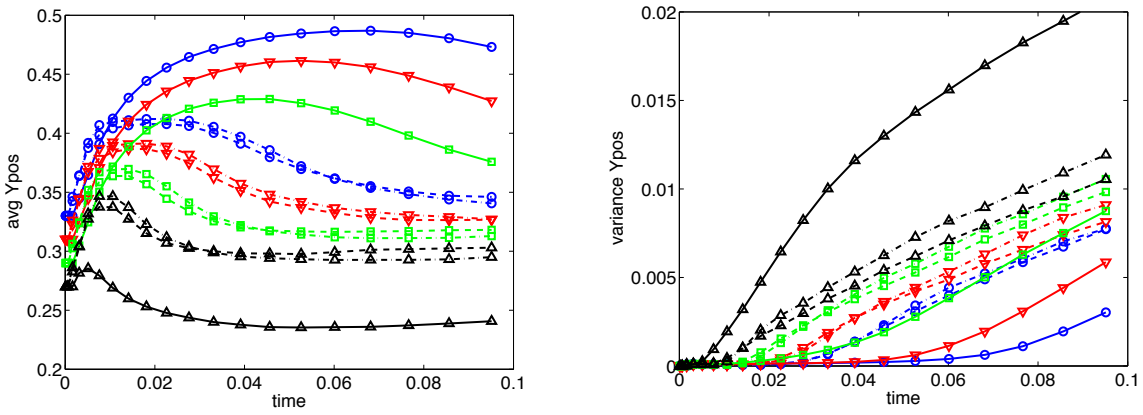

Figure 24. Average (left) and variance (right) particle positions for far-side particles. From the far field to the jet, particle initial locations are denoted with blue circles ($y_0 = +2.07R_j$), red gradients ($y_0 = +1.8R_j$), green squares ($y_0 = +1.53R_j$) and black triangles ($y_0 = +1.27R_j$). Particle time scales are denoted by line pattern with solid denoting $\tau_p = \tau_h =$ 3e-2 s, dash-dot denoting $\tau_p = \tau_h =$ 3e-3 s and dashed denoting $\tau_p = \tau_h =$ 3e-5 s.

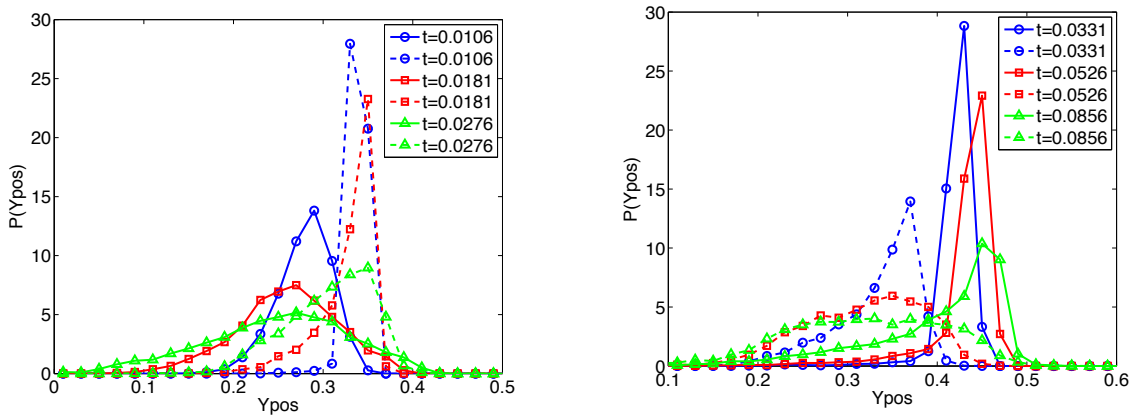

Figure 25. Particle position PDFs for particles with $y_0 = +1.27R_j$ (left panel) and $y_0 = +1.53R_j$ (right panel) at various evolution times. Small particles ($\tau_p = \tau_h =$ 3e-5 s) denoted with dashed lines while large particles ($\tau_p = \tau_h =$ 3e-2 s) denoted by solid lines. Note that times for different particles will differ because of the times at which the plume interacts with them.

Gas temperatures observed by particles around the hot jet

To predict the particle temperatures, it is first necessary to understand the temperature environment to which the particles are exposed. In the previous subsection the particle position distribution was described. This particle distribution is relative to a temperature field distribution. That is, both the particle position and the temperature at that position are random variables. It becomes challenging to represent these successive levels of random variables so we present here simply the statistics for a given class of particles, those starting at the same initial condition with the same properties (τ_p and τ_h).

In Figure 26 the average and root mean square gas temperatures observed by wall-side particles are plotted. These quantities are obtained by querying the environment experienced by each particle over its history. Particles that are nearer the jet initially are entrained earlier and experience higher temperatures as the jet is less diluted at those times; the rms fluctuations are also commensurately larger. For the wall-side particles there is little difference in the temperature environment observed by larger versus smaller particles. While there are measurable differences in the average positions and dispersion in Figure 22,

these do not translate into significant differences in the observed average gas temperature. There is some correlation between the rms fluctuations in the gas temperature and those of position. Representative PDFs for the particle-observed gas temperature are shown in Figure 26. Statistics for a given particle initial location and properties are collected for the curves here so that the PDF would be written $P(T_g|$ $y_0, \tau_p, \tau_h)$, that is the statistics are conditional on the particle initial location and properties.

The temperature evolution shows certain characteristics that are common to all particle classes. All particles here originate at ambient temperature. As the jet mixes with the surrounding air, particles are entrained and rapidly heated. The PDF is highly skewed in the early period with a delta function at ambient and long tail toward higher temperatures. The highest temperatures tend to be reached in the early stages because the hot jet is subsequently diluted, reducing the maximum temperatures. The observed temperature PDF then develops a mode at temperatures above ambient as the extremes of temperature are mixed out. This mode grows and narrows with time, subject to drift associated with large scale mixing.

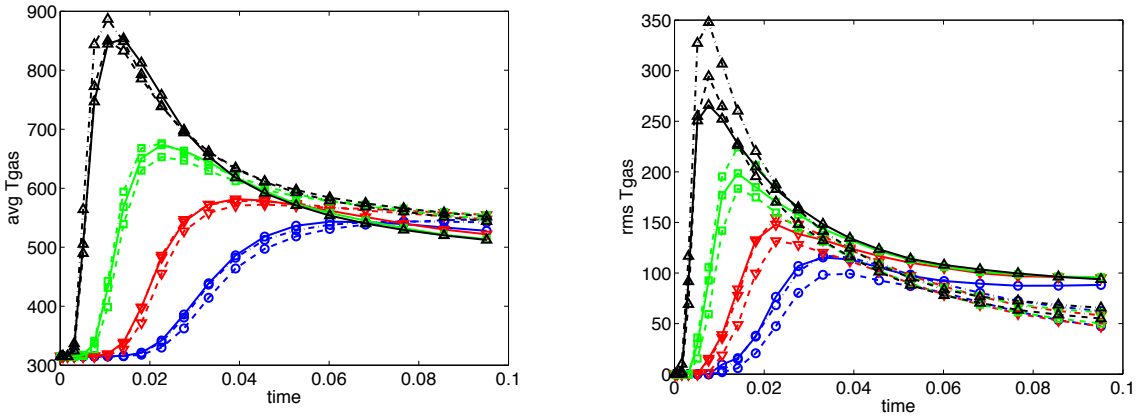

Figure 26. Average (left) and rms (right) observed gas temperatures for wall-side particles. From the wall to the jet, particle initial locations are denoted with blue circles ($y_0 = -2.07R_j$), red gradients ($y_0 = -1.8R_j$), green squares ($y_0 = -1.53R_j$) and black triangles ($y_0 = -1.27R_j$). Particle time scales are denoted by line pattern with solid denoting $\tau_p = \tau_h =$ 3e-2 s, dash-dot denoting $\tau_p = \tau_h =$ 3e-3 s and dashed denoting $\tau_p = \tau_h =$ 3e-5 s.

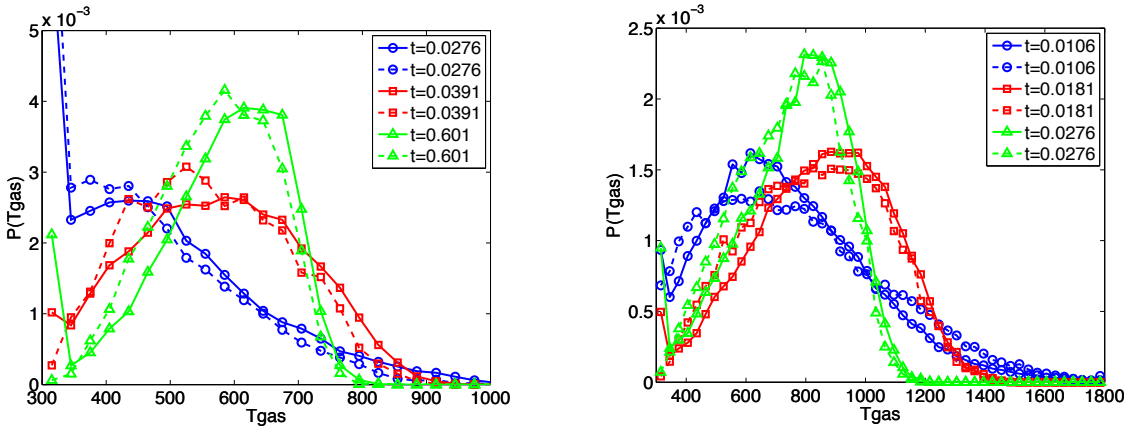

Figure 27. Observed gas temperature PDFs for particles with $y_0 = -1.8R_j$ (left panel) and $y_0 = -1.27R_j$ (right panel) at various evolution times. Small particles ($\tau_p = \tau_h =$ 3e-5 s) denoted with dashed lines while large particles ($\tau_p = \tau_h =$ 3e-2 s) denoted by solid lines. Note that times for different particles will differ because of the times at which the plume interacts with them.

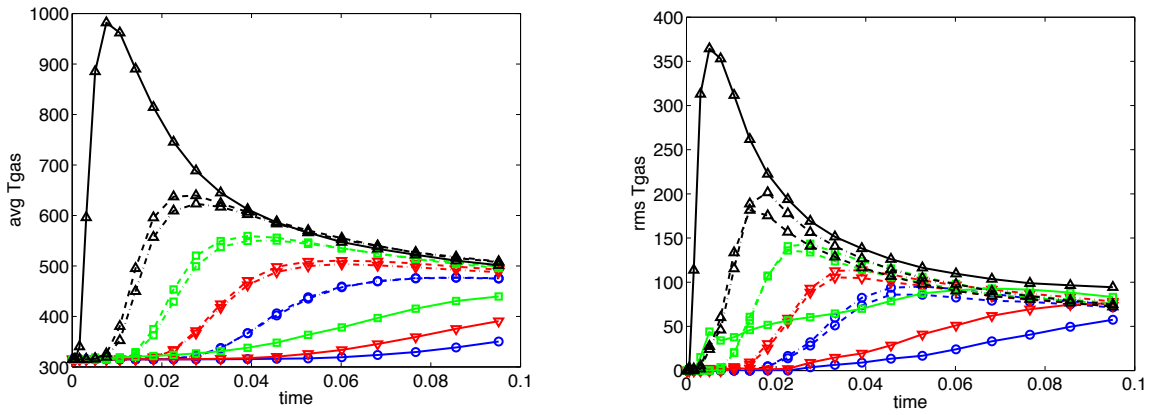

Figure 28. Average (left) and variance (right) observed gas temperatures for far-side particles. From the far field to the jet, particle initial locations are denoted with blue circles ($y_0 = +2.07R_j$), red gradients ($y_0 = +1.8R_j$), green squares ($y_0 = +1.53R_j$) and black triangles ($y_0 = +1.27R_j$). Particle time scales are denoted by line pattern with solid denoting $\tau_p = \tau_h =$ 3e-2 s, dash-dot denoting $\tau_p = \tau_h =$ 3e-3 and dashed denoting $\tau_p = \tau_h =$ 3e-5 s.

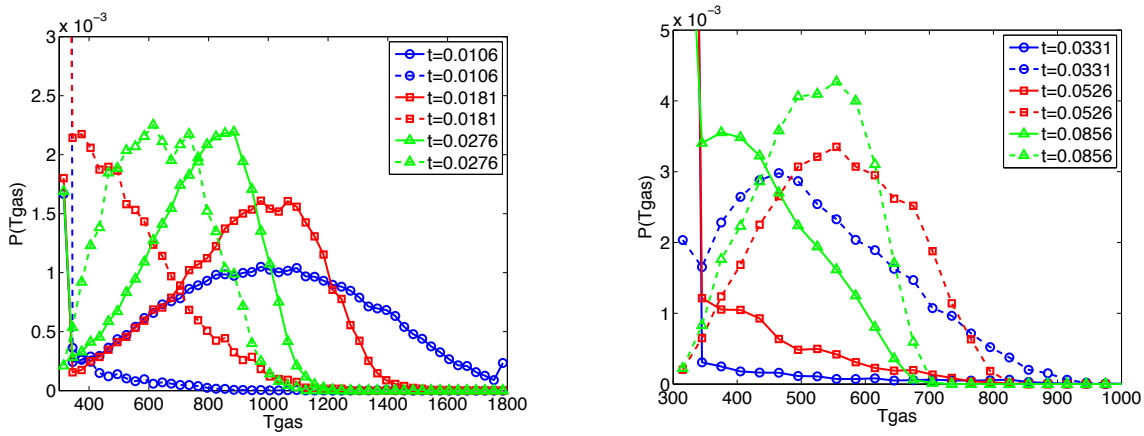

Figure 29. Observed gas temperature PDFs for particles with $y_0 = +1.27R_j$ (left panel) and $y_0 = +1.53R_j$ (right panel) at various evolution times. Small particles ($\tau_p = \tau_h =$ 3e-5 s) denoted with dashed lines while large particles ($\tau_p = \tau_h =$ 3e-2 s) denoted by solid lines. Note that times for different particles will differ because of the times at which the plume interacts with them.

For the far-side particles similar quantities are also plotted. Figure 28 shows the mean and rms observed gas temperatures as a function of the particle type and initial position. In accord with the differences in the average and rms particle positions shown in Figure 24 for the large and small particles, there are significant differences in the particle-observed gas temperatures associated with the expected particle locations. This is true for both the average temperature and fluctuations. The PDFs of temperatures for far-side particles closer to the jet are shown in Figure 29.

As indicated at the start of this subsection, both the particle position and the temperature at each position are random variables. The PDFs plotted in Figure 26 and Figure 29 are thus related to the joint conditional PDFs for temperature at a position and for the position given the original particle state, $P(T_g|\, y_0, \tau_p, \tau_h) = P(T_g|\, y_{\rm pos})\, P(y_{pos}|\, y_0, \tau_p, \tau_h)$; the latter term is that shown in Figure 23 and Figure 25 while the first term on the right-hand side is given for reference at selected positions in Figure 30. Thus the PDF obtained from the Lagrangian particle statistics in Figure 26 and Figure 29 are obtainable from the

combinations of those in Figure 23 and Figure 25 with Figure 30. Consideration of the PDFs shows that the variation in both quantities is significant. This is an important point to note in carrying out CFD simulations. While stochastic models of dispersion are common in the context of CFD, accounting for the stochastic variation in temperature is not typical.

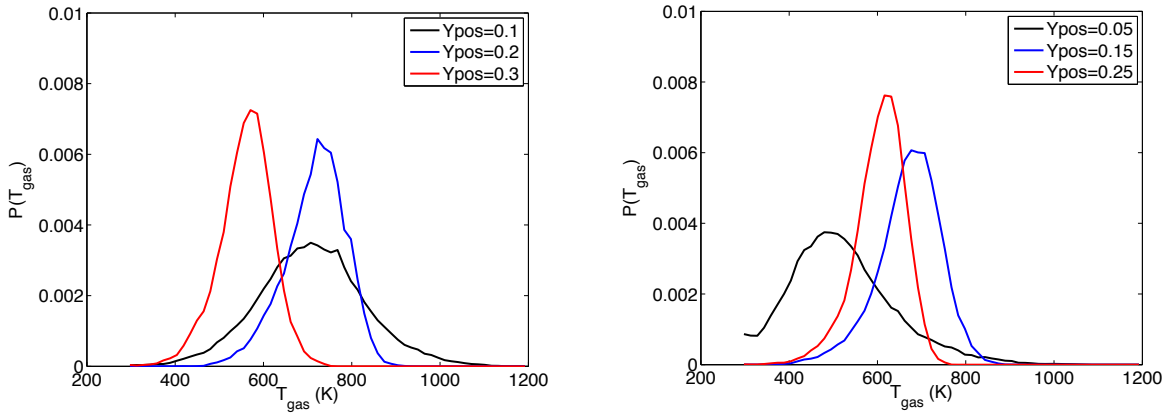

Figure 30. Gas temperature PDFs at indicated positions across the ODT domain at a time of 0.02 s.

Particle temperatures as a function of particle time scales and relative position

The previous two subsections have addressed the particle dispersion and the temperature fields associated with the particles. A later subsection will address various interaction times and the relative motion between particles and the gas phase. In this subsection, we address the particle temperatures, the integrated effect of the particle-observed environment, integrated using Eq. (1).

Since there are many similarities between the particle temperatures presented here and the particle-observed gas temperatures in the previous subsection, the discussion here will be abbreviated. Figure 31 and Figure 32 show the average and rms particle temperatures for the wall-side and far-side particles, respectively; these can be compared with Figure 26 and Figure 28. The PDFs of selected particle temperatures are shown in Figure 33 and Figure 34 for the wall-side and far-side particles; these can be compared with particle-observed gas temperature PDFs in Figure 27 and Figure 29.

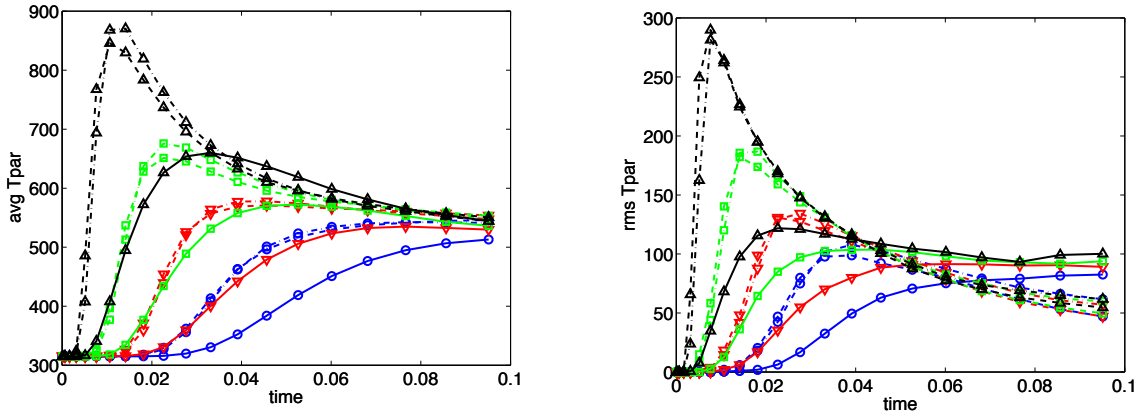

Figure 31. Average (left) and rms (right) temperatures for wall-side particles. From the wall to the jet, particle initial locations are denoted with blue circles ($y_0 = -2.07R_j$), red gradients ($y_0 = -1.8R_j$), green squares ($y_0 = -1.53R_j$) and black triangles ($y_0 = -1.27R_j$). Particle time scales are denoted by line pattern with solid denoting $\tau_p = \tau_h$ = 3e-2 s, dash-dot denoting $\tau_p = \tau_h$ = 3e-3 s and dashed denoting $\tau_p = \tau_h$ = 3e-5 s.

Particle temperatures are initially all at ambient, and as they are entrained by the hot jet they are heated. Particles closer to the jet are entrained earlier before the jet has been substantially diluted, penetrate further into the jet on average and experience hotter gas temperatures for both of these reasons. For the smaller classes of particles the temperatures follow the gas temperature statistics presented in the previous section. For larger particles where the particle time scale will be seen to be large relative to the turbulence time scales, the particle temperatures significantly lag the gas temperature as seen with the solid curves in Figure 31 and Figure 32. Similarly, the PDFs for the larger particles are narrower and limited to lower temperatures because the heating time scale is comparable to the evolution time. In Figure 21 it was shown that the moderate time scale particles, ($\tau_p = \tau_h$ = 3e-3 s), acted to significantly filter high frequency temperature fluctuations and these differences appear in comparing the gas and particle temperature PDFs. However, it is interesting that these differences are not evident in the first and second moments.

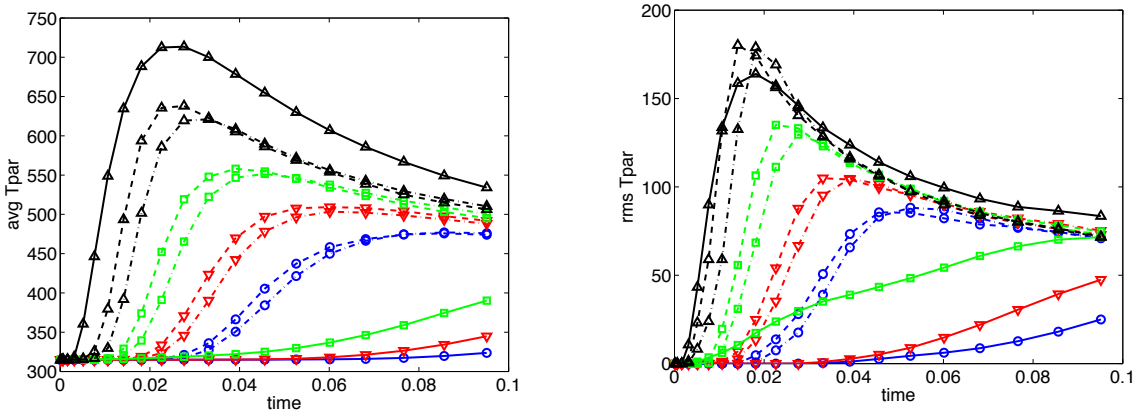

Figure 32. Average (left) and variance (right) temperatures for far-side particles. From the far field to the jet, particle initial locations are denoted with blue circles ($y_0 = +2.07R_j$), red gradients ($y_0 = +1.8R_j$), green squares ($y_0 = +1.53R_j$) and black triangles ($y_0 = +1.27R_j$). Particle time scales are denoted by line pattern with solid denoting $\tau_p = \tau_h$ = 3e-2 s, dash-dot denoting $\tau_p = \tau_h$ = 3e-3 s and dashed denoting $\tau_p = \tau_h$ = 3e-5 s.

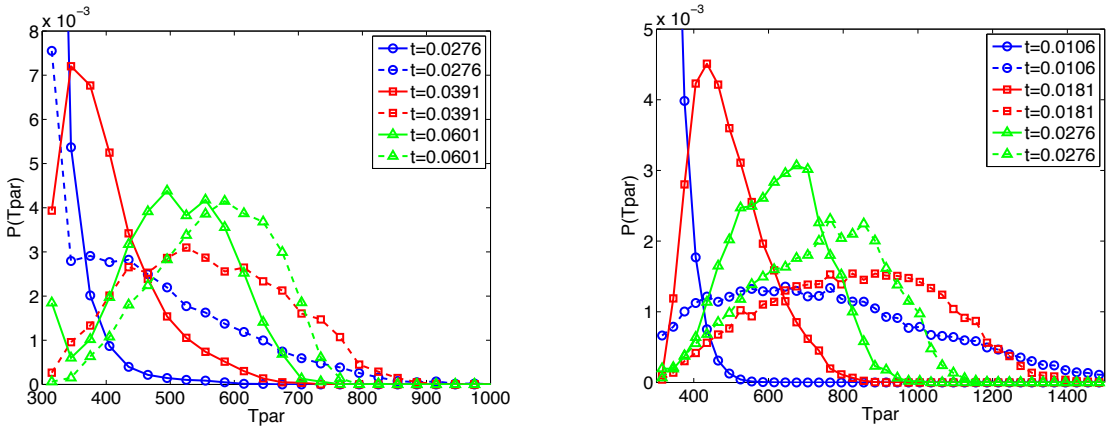

Figure 33. Observed particle temperature PDFs for particles with $y_0 = -1.8R_j$ (left panel) and $y_0 = -1.27R_j$ (right panel) at various evolution times. Small particles ($\tau_p = \tau_h$ = 3e-5 s) denoted with dashed lines while large particles ($\tau_p = \tau_h$ = 3e-2 s) denoted by solid lines. Note that times for different particles will differ because of the times at which the plume interacts with them.

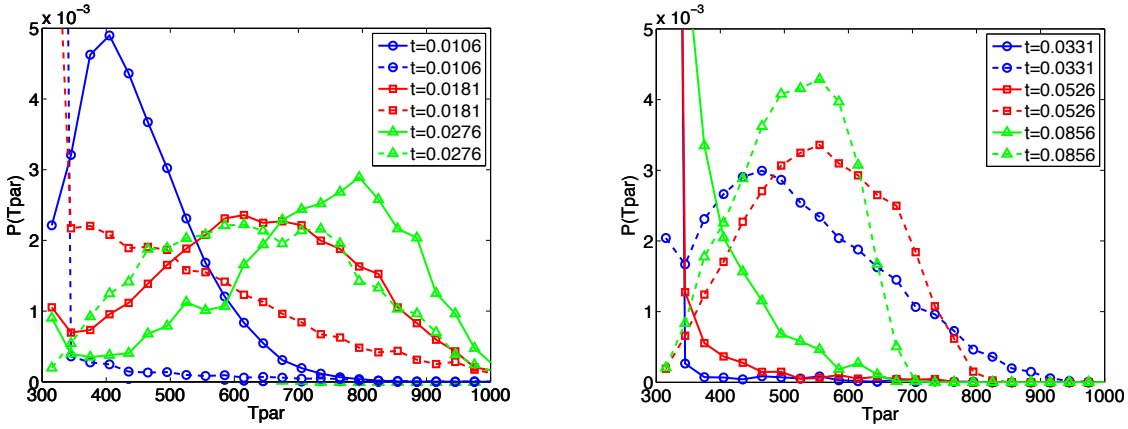

Figure 34. Observed particle temperature PDFs for particles with $y_0 = +1.27R_j$ (left panel) and $y_0 = +1.53R_j$ (right panel) at various evolution times. Small particles ($\tau_p = \tau_h$ = 3e-5 s) denoted with dashed lines while large particles ($\tau_p = \tau_h$ = 3e-2 s) denoted by solid lines. Note that times for different particles will differ because of the times at which the plume interacts with them.

For the larger far-side particles shown in Figure 32 and Figure 34, the differences in the particle position continue to be significant. The larger particles initiated at $y_0 = +1.27R_j$ are entrained within the high-temperature regions of the jet to a greater degree than the smaller particles (c.f. Figure 28) and the resulting particle temperature exceeds that of the smaller particles because of the differences in the particle trajectory. Conversely, the larger particles initiated at $y_0 \geq +1.53R_j$ are not entrained in the jet until much later; the dilatational flow discussed around Figure 24 causes the trajectory of those particles to move beyond the bounds of the jet until later times.

Maximum particle temperatures as a measure of neutralization

A primary objective of this work is to develop capabilities that are useful in understanding the probability that particles exposed to high temperature environments are neutralized. While the actual mechanism by which particles are neutralized is uncertain, research suggests that some heat transfer to internal regions of the particle are important and the heating and vaporization of water probably are significant [4]. In particular, vaporization of water or any chemical process is likely to introduce some nonlinearities into the particle heating process. We have not tried to capture any of these nonlinearities potentially associated with particle neutralization in the present work. Instead, we measure the maximum particle temperature statistics under a fixed particle specific heat assumption as a representative quantity. Since the particle temperature in the present mode follows the linear Eq. (1), short time scales at high temperatures are not expected to be significant with this model; nonlinear heating can be, for example, more sensitive to short periods of time at high temperatures.

Distributions of the maximum particle temperature observed are shown in Figure 35. These show the reduced temperatures reached by the large particles due to finite heating rates. The substantial temperature differences of the large particles on the far-side (last three panels) are associated with the different particle trajectories discussed above. The maximum temperature PDFs are narrower than the instantaneous particle temperature PDFs shown in the previous subsection since this selects only the maximum temperature for each particle and leaves out the variation in individual particle histories.

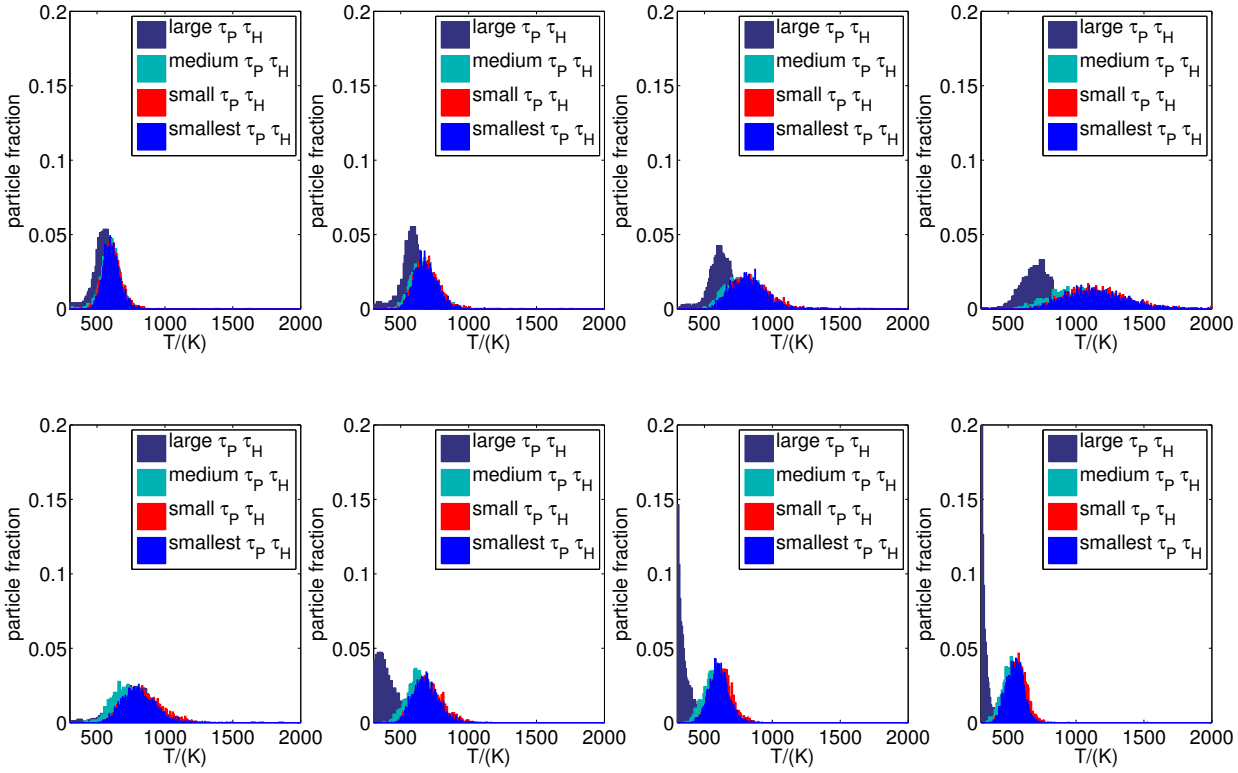

Figure 35. Maximum particle temperature PDFs. Top row shows wall-side particles with $y_0 = -2.07R_j$ (left panel), $y_0 = -1.8R_j$, $y_0 = -1.53R_j$ and $y_0 = -1.27R_j$ (right panel). Bottom row shows far-side particles with $y_0 = +1.27R_j$ (left panel), $y_0 = +1.53R_j$, $y_0 = +1.8R_j$ and $y_0 = +2.07R_j$ (right panel). Particle sizes are separated by one order of magnitude with smallest particles ($\tau_p = \tau_h$ = 3e-5 s), small particles ($\tau_p = \tau_h$ = 3e-4 s), medium particles ($\tau_p = \tau_h$ = 3e-3 s) and large particles ($\tau_p = \tau_h$ = 3e-2 s).

The interesting question is not necessarily what the distribution of temperatures is, but rather what the cumulative fraction of particles is that were not heated above some critical temperature. The integral of the PDFs shown here, the cumulative distribution functions (CDFs), provide that information and these are presented for selected particles in Figure 36. These plots make it easy to select the fraction of the distribution for which a specific criterion is met or not met. For example, the fraction of particles that are below 600 K can be found by reading off the vertical line added to Figure 36. For some particle classes a small fraction are below 600 K while for other particle classes most are below this criterion.

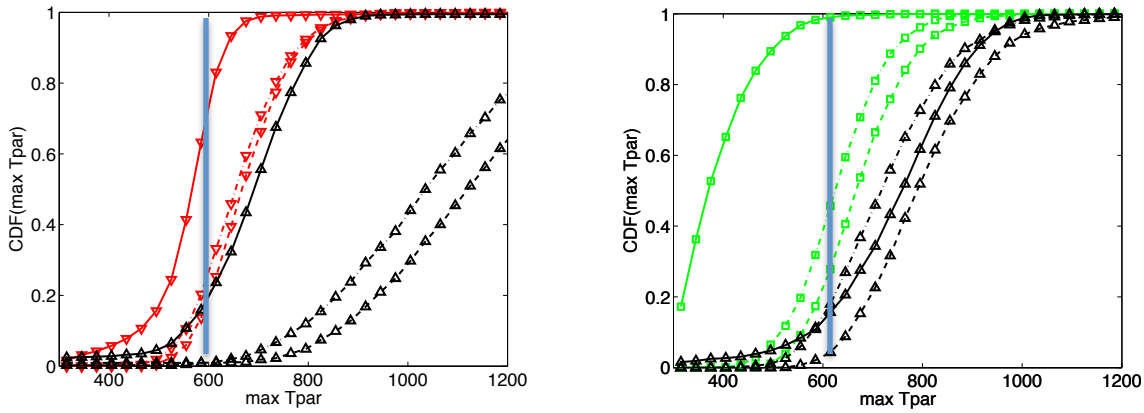

Figure 36. Cumulative distributions of the maximum particle temperature. Wall side particles are shown in the left panel with red gradients ($y_0 = -1.8R_j$) and black triangles ($y_0 = -1.27R_j$). Far side particles are shown in the right panel with green squares ($y_0 = +1.53R_j$) and black triangles ($y_0 = +1.27R_j$). Particle time scales are denoted by line pattern with solid denoting $\tau_p = \tau_h$ = 3e-2 s, dash-dot denoting $\tau_p = \tau_h$ = 3e-3 s and dashed denoting $\tau_p = \tau_h$ = 3e-5 s. Vertical lines drawn near 600 K provide a guide for reading the fraction below that temperature.

Lagrangian particle time scales

The transient nature of turbulence can be represented in a variety of ways. The statistics presented thus far represent only single points in time (except for the maximum particle temperature). A common approach for characterizing the time scales for fluctuations in turbulence is the two-time correlation, presented here for the temperature fluctuations,

$$R_{T_g}(t,s) = \frac{\left\langle T_g'(t) T_g'(t+s) \right\rangle}{\left\langle T_g'(t)^2 \right\rangle^{1/2} \left\langle T_g'(t+s)^2 \right\rangle^{1/2}} \tag{11}$$

where primes indicate the quantity is the fluctuation about the local mean, angle brackets indicate ensemble averaging, t is one time and s is the separation time. A smaller correlation coefficient indicates greater differences in the temperature over that separation time. The correlation coefficient is plotted for the largest and smallest size class of the wall-side particle nearest the jet in Figure 37. Correlation coefficients are computed in the forward and backward time directions with six times shown in Figure 37; the curves peak at unity at the time where they are centered. The correlation coefficients are narrow early in time and are stretched as the time evolves. This reflects the evolution of the turbulent time scale. Of interest here is the fact that the larger particles with the longer time scales have narrower correlation coefficients, especially for short separation times where the profiles for the large particles are particularly peaked. The reasons for this will be investigated in the subsequent subsection.

The integral time scale is defined as the integral over the correlation coefficient either for all time up to the current or from the current time forward

$$\tau_{L,int} = \int_0^t R(t,\tau)\,d\tau \quad \text{or} \quad \int_t^\infty R(t,\tau)\,d\tau \quad , \tag{12}$$

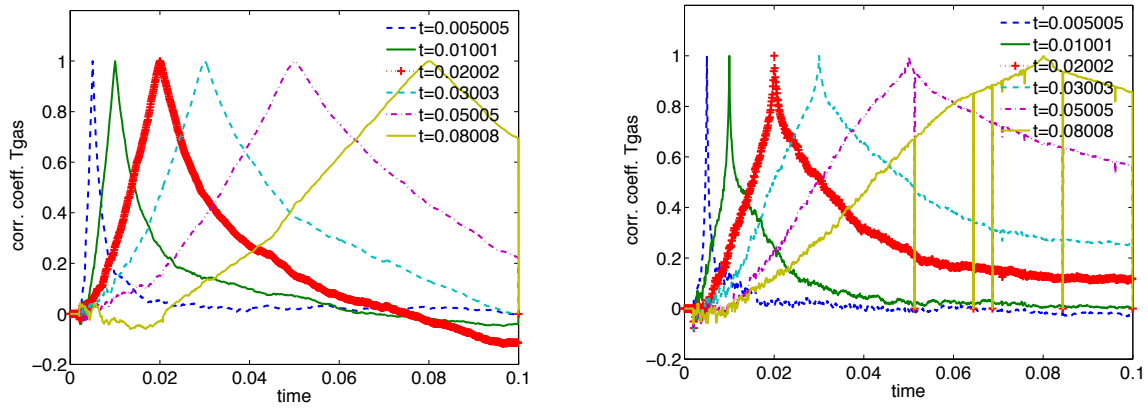

Figure 37. The correlation coefficient, Eq. (11), for particles initially at $y_0 = -1.27R_j$. The left panel shows results for small particles with $\tau_p = \tau_h$ = 3e-5 s and the right panel shows results for large particles with $\tau_p = \tau_h$ = 3e-2 s. (Spurious values visible at right are a consequence of particles sticking to the wall.)

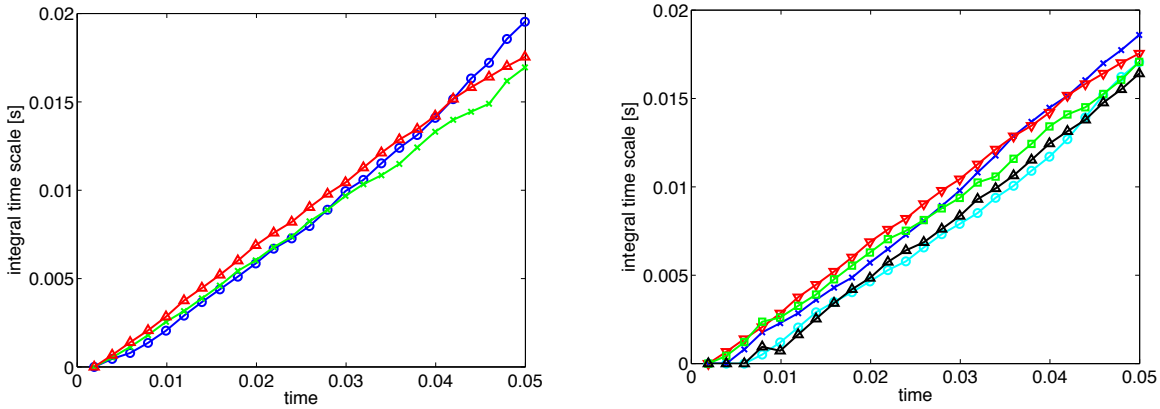

Figure 38. Lagrangian integral time scales for temperature computed using Eq. (12). The left panel shows results for particles initially at $y_0 = -1.27R_j$ with blue circles for large particles ($\tau_p = \tau_h$ = 3e-2), green + for $\tau_p = \tau_h$ = 3e-3 and red triangles for small particles ($\tau_p = \tau_h$ = 3e-5). The right panel shows integral time scales for small particles ($\tau_p = \tau_h$ = 3e-5) with different initial positions: cyan circles ($y_0 = -1.8R_j$), blue x ($y_0 = -1.53R_j$) red gradients ($y_0 = -1.27R_j$), black triangles ($y_0 = +1.53R_j$) and green squares ($y_0 = +1.27R_j$).

where the subscript L indicates that this is a Lagrangian time scale associated with the particles. In the present work the first definition with the integral over the time before t is used because we are interested in the cumulative heating time to a point. In addition, the statistics do not continue for sufficiently long to carry out the second integral (nominally to infinity or until the correlation is effectively zero) for times beyond 0.02. The integral time scale computed using Eq. (12) is plotted in Figure 38 both for various particle sizes using the initial location from Figure 37. In general the integral time scales increase linearly in time as is expected. It is also seen that the narrowing of the peaks has a relatively small effect on the integral time scale.

While larger particles have initially smaller integral scales, as observed in Figure 38, the effect is small relative to the linear growth in the integral time scale. For the right panel in Figure 38 the most significant factor is the initial entrainment time that determines when the time correlation starts to grow with the approximately linear growth after the initial transient. Thus particles initially nearer the jet that are entrained earlier have larger integral time scales at any given time. The particle time scales are of the

same magnitude but longer than the integral time scales computed using the typical k-ε parameters as was done in Figure 20. This is typical of Lagrangian statistics [23]. This latter point suggests the potential discontinuities associated with ODT triplet maps are not adversely affecting these statistics.

Time scales for particle-turbulence interactions

As discussed in the Introduction, the interactions of particles with the temperature field are affected by three phenomena: the overall evolution of the gas temperature field, the relative motion of the particles through the temperature field as indicated by Eq. (4) and the diffusion of the temperature field relative to the particles as indicated by Eq. (6). The integral time scale discussed in the previous section characterizes the evolution of the temperature field. This leads us to examine two distributions introduced in Eqs. (8) and (9); these are the distributions of the rates of particle-observed gas-phase temperature change due to particle slip through varying temperature fields and due to diffusion of the temperature field. The ODT model provides a unique opportunity to quantify these distributions because of its resolution of the full range of length scales up to relatively large Reynolds numbers.

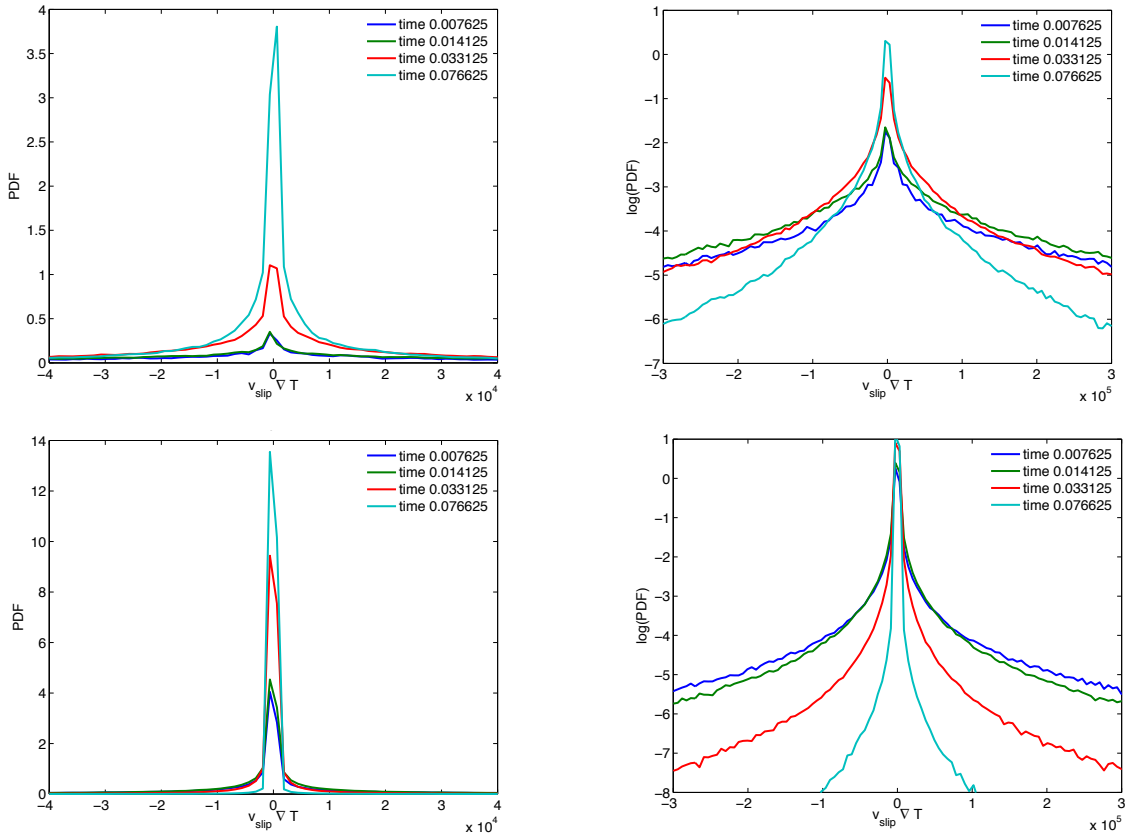

Figure 39. Probability density functions of the time scales associated with particle slip across temperature gradients for particle $y_0 = -1.27R_j$. The upper panels show particles with $\tau_p = \tau_h$ = 3e-2 s and the lower panels show particles with $\tau_p = \tau_h$ = 3e-5 s. The left panels show the PDF and the right panels show the logarithm of the same PDF.

We first discuss the distribution of the temperature rate of change associated with the motion of particles through the temperature field discussed around Eqs. (4) and (8), $P\left(\left(\Delta t\right)^{-1}\right) = P\left(\left(v_p - v_g\right)\nabla T_g\right)$, plotted in Figure 39. This PDF is plotted in the left column for large particles (top row) and small particles (bottom row). Plotted in this coordinate system, the PDF has a large peak near zero with long tails.

These tails are easier to visualize if the logarithm of the probability is plotted as in the right panels of Figure 39. It is evident that rates of temperature change are strongly intermittent. The intermittency is indicated in the figure by the strong central peak where the rate is near zero, with infrequent but not insignificant probability at high and low values. Turbulent flows are characterized by such intermittency with fine-scale but intense dissipation structures. This intermittency is strongest when the fluid time scales are small relative to the particle time scales, corresponding to the particles moving through fluid structures rather than being carried with them. This is determined by considering the distribution for the large particles (top row, Figure 39) where the fluid time scales are small until near the end of the simulation. For the smaller particles (bottom row, Figure 39) the intermittency decreases (distribution is less wide at the tails) as the time scale ratio $\boldsymbol{\tau}_{L,int}/\boldsymbol{\tau}_p$ gets larger.

For intermittent processes like those shown in Figure 39 it is sometimes advantageous to look at the logarithm of the rates. To do this, we separate the positive and negative values and compute the PDF of the logarithm of each; these PDFs are plotted in Figure 40 from which several points can be learned. First, the PDFs for the positive and negative rates of change (solid and dashed lines, respectively) are very close, showing that there is significant symmetry. Naturally there must be some overall evolution of the system, but the random motions associated with turbulence dwarf this, implying that the turbulence timescales are small compared to the flow evolution timescale. Second, for particles and times where the time scale ratio $\tau_{L,int}/\tau_p$ gets larger there is significant reduction in the magnitude of the fluctuations, indicated in the migration of the PDFs to lower values at later times, which is consistent with the narrowing of the PDFs in time in Figure 38. This is expected because these smaller particles are approaching the small Stokes number limit where there is little slip. These variations can be further quantified by looking at the statistics for the moments of these distributions. In Figure 41 the averages corresponding to the logarithmic PDFs plotted in Figure 40 are shown, quantifying the reduction in the magnitude of the rates with time.

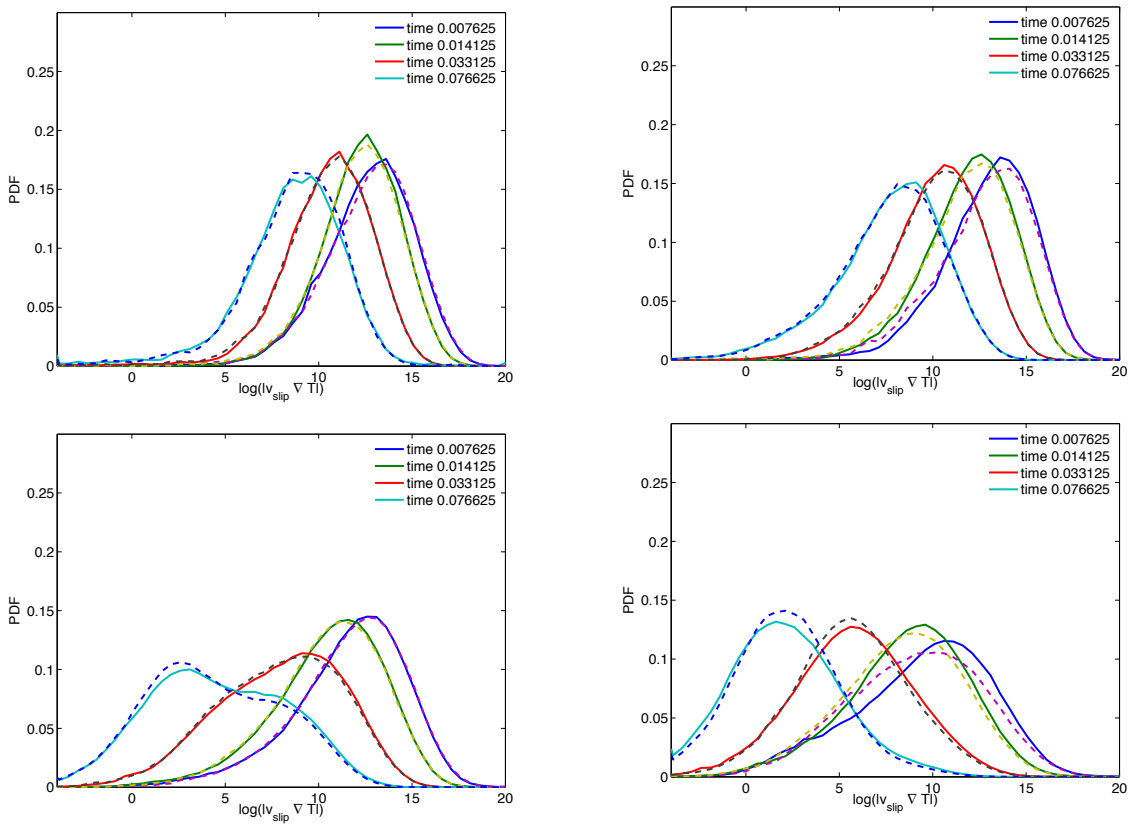

Figure 40. Probability density functions of the time scales associated with particle slip across temperature gradients for particle $y_0 = -1.27R_j$. Positive rates of temperature change are plotted with solid lines and absolute values of negative rates of change are plotted with dashed lines. The upper left panel shows particles with $\tau_p = \tau_h$ = 3e-2 s, upper right shows particles with $\tau_p = \tau_h$ = 3e-3 s, lower left shows particles with $\tau_p = \tau_h$ = 3e-4 s and the lower right panel shows particles with $\tau_p = \tau_h$ = 3e-5 s.

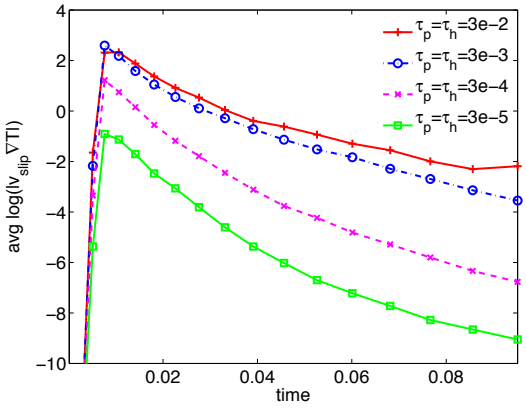

Figure 41. Average of the logarithm of $|v_{slip}\nabla T|$ for particle $y_0 = -1.27R_j$.

In addition to the motion of the particles relative to the temperature field, the particles will observe temperature changes associated with the diffusional evolution of the temperature field. The distribution of these time scales, $P\left(\left(\Delta t\right)^{-1}\right) = P\left(\nabla\cdot\left(D\nabla T_g\right)\right)$, are shown in Figure 42 for the same conditions as

presented in Figure 39. There are similarities in the form of the distribution for these two quantities, with both exhibiting a strong peak roughly symmetric around zero with strong intermittency indicated by the long tails. When the logarithm of the PDF is plotted in the right panels of Figure 42 the magnitudes of these tails are similar for a given evolution time regardless of differences in particles size. As above, we plot the logarithm of the absolute values of these diffusional rates of change in Figure 43; these can be compared with those for the rate of temperature change due to relative motion in Figure 40. Again, these plots of the logarithm of the time scale show little variation with particle size. This is expected because the quantity plotted is associated only with the gas-phase diffusion and not dependent upon the particle size as is the slip velocity.

The results for the rate of change of temperature shown in this subsection show similarities with recent statistical analyses of velocity increments of Lagrangian particles and their acceleration [24]. In these studies new approaches to measure acceleration and the velocity increments show strong intermittency and long tails; such statistics deviate from expectations given the classical Kolmogorov theory. In that work a multi-fractal model has been suggested as providing a possible description of the properties of these fields.

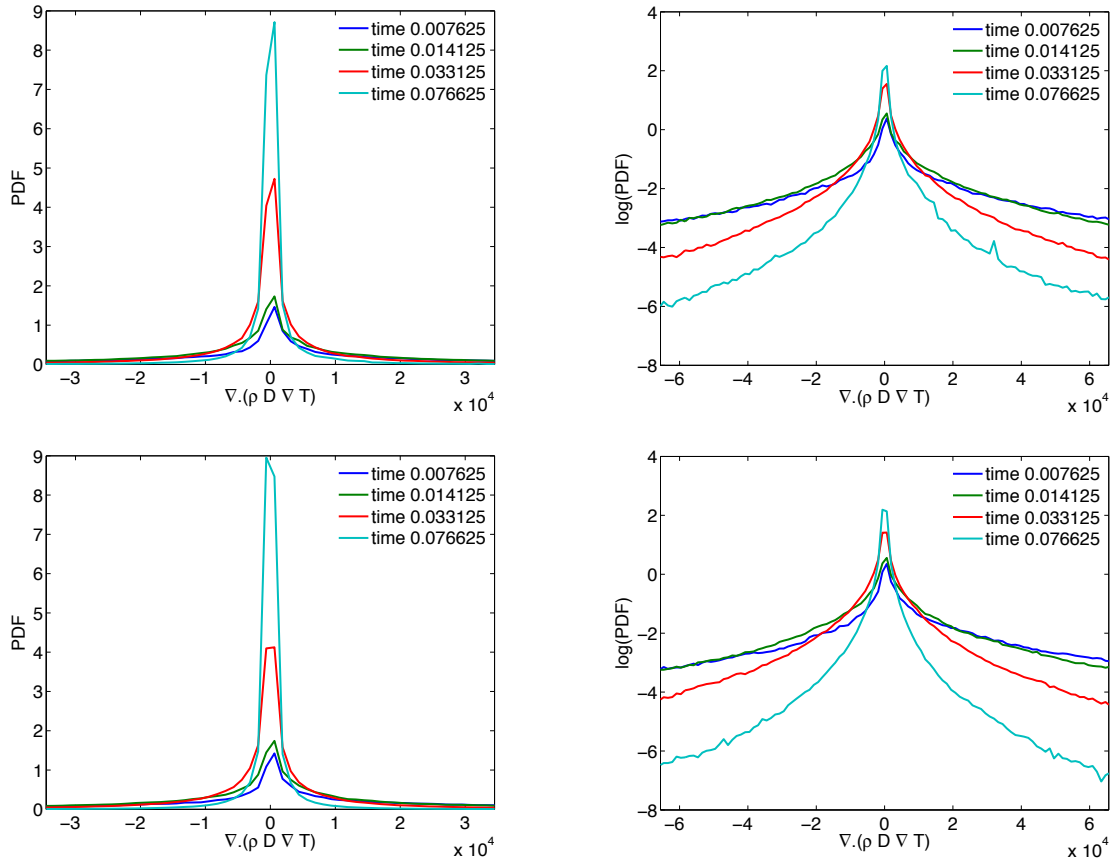

Figure 42. Probability density functions of the time scales associated with temperature diffusion for particle $y_0 = -1.27R_j$. The upper panels show particles with $\tau_p = \tau_h$ = 3e-2 s and the lower panels show particles with $\tau_p = \tau_h$ = 3e-5 s.

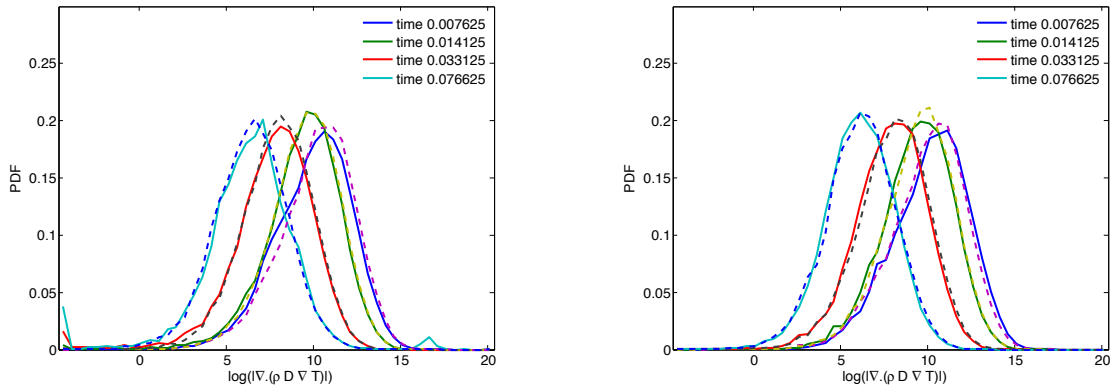

Figure 43. Probability density functions of the logarithms of time scales associated with temperature diffusion for particle $y_0 = -1.27R_j$. Positive rates of temperature change are plotted with solid lines and absolute values of negative rates of change are plotted with dashed lines. The left panel shows particles with $\tau_p = \tau_h$ = 3e-2 s and the right panel shows particles with $\tau_p = \tau_h$ = 3e-5 s.

Summary of results for particles in a wall-bounded hot jet

Several factors play a role in determining the temperature histories for particles interacting with high temperature gases. First, the relative locations and dispersion of particles relative to the dispersion of the hot gases is important. Particles that do not mix with the hot gases until the gases are appreciably diluted are limited in the heating to which they can be exposed. The varying radial distributions used in this section show the significance of this.

When the particle heating and momentum interaction time scales are large relative to the integral scales, finite transport effects are significant. The large particles used in the present study had significantly altered mean motion and dispersion as well as significantly reduced heating rates.

When there is a bulk flow, as occurs on the far side for the hot jet associated with domain dilatation, the particle interaction with this bulk flow can significantly affect the time that it interacts with the hot gases. For the particles that were closest to the hot jet, they responded less to the bulk flow and were rapidly entrained while particles farther away followed trajectories that delayed their interaction with the hot jet. Such bulk flows might occur when blasts are followed by additional heat release associated with metal particle combustion as occurs in some explosives.

The statistics of three different time scales were discussed. The particle-observed temperature autocorrelation is used to determine a Lagrangian integral time scale. These time scales increase linearly after the turbulence has developed around the particles as is appropriate for this flow field. Because the integral scale is largely a function of the flow, there is relatively little dependence on the particle parameters. However, the ratio of the particle time to the integral time determines the extent to which particles keep up with gas temperature fluctuations. In the present simulations, the largest particle class significantly lags at the scale of the overall flow evolution. Intermediate and smaller particles will not follow the fastest fluctuations but do follow the evolution of the average gas temperatures; this is sufficient to see little difference among these particles in terms of particle temperature statistics.

Other time scales can be associated with the actual rates of particle-observed gas-phase temperature change. There is a time scale associated with particles moving relative to the fluctuating gas temperature

field and there is one associated with the diffusional changes in the gas-phase temperature. The distributions of both of these time scales are roughly symmetric about zero, but are strongly intermittent. The distributions of the logarithms of their absolute values exhibit more normal distributions. These time scales are a function of the gas-phase diffusive scales since they involve gradients and the scale involving the relative motion will also depend on the particle Stokes number.

Summary

This report describes an approach to predict the statistics of particle time-temperature histories relevant to neutralization of particles through exposure to high temperature environments. To collect the statistical quantities of interest, we employ the ODT model. Lagrangian particle tracking has been implemented within the context of ODT to allow collection of statistics for particles that move relative to fluid elements (finite slip velocities), and this implementation has been evaluated through predictions of classical particle dispersion results. Within the current project year we have made several extensions to the Lagrangian particle models within the ODT model. These include differentiating between continuous and instantaneous actions of the turbulent eddies on the particle and two-way coupling between the particle and fluid momentum. Incorporating Lagrangian particles into the ODT model introduces one additional parameter relating the eddy rate to the eddy lifetime, and we characterized this parameter through an extensive sensitivity analysis.

To evaluate the performance of the ODT Lagrangian particle modeling capabilities, we have carried out a series of simulations for which there is experimental data available for comparison purposes. This includes particle dispersion in homogeneous decaying turbulence, isothermal jets, turbulence development in particle-laden jets where two-way coupling is important and deposition of particles onto channel walls in channel flow. In general, the performance of the ODT model has been adequate in each of these cases. While not discussed in this report, evaluation of model performance in each of these configurations has provided some further insight into the model and has guided further model refinement as discussed in our publication [8].

To evaluate particle time temperature histories, we carried out simulations of a non-isothermal jet that spreads to interact with particles; the flow is bounded on one side by a wall and unbounded on the other with particles distributed regularly outside the initial jet region. Ranges of particle properties were provided so that particle momentum and thermal response ranged from fast (following fluid elements) to slightly slower than the integral scales. First and second moments along with PDFs of the particle dispersion, the particle-observed gas temperature, the particle temperature and maximum temperature were all reported. Particle Lagrangian temperature autocorrelations were used to compute integral time scales. Time scale distributions associated with the rate of temperature change were determined for both changes associated with particles moving relative to the temperature field and changes associated with diffusional mixing of the temperature field. The following points are worthy of note:

- Dilatation induced significant flow, and this was a key determinant in different statistics developing for large particles. In results not shown here, we note that the role of dilatation in altering statistics for larger particles was more significant in combusting flows with greater dilatation.
- Inhomogeneous turbulence significantly affected the particle dispersion as some particles were dispersed into high turbulence regions interior to the jet while others were dispersed to low turbulence regions near the jet edge.
- Differences in particle dispersion led to differences in all other statistics due to differences in the interaction of the particles with the dispersing jet.
- Particle-observed temperatures (the gas temperature environment that the particle experienced) for a given particle class were a combination of the stochastic variations in particle dispersion and jet dispersion, the latter leading to the temperature PDF at a point. Both components were significant.

- Particle temperatures were affected primarily by dispersion except for the largest particle class where finite-rate heating was significant. The largest particle class had heating time scales slightly longer than the integral time scales. Rapid temperature fluctuations were observed in PDFs but were not reflected in lower moments.
- Lagrangian gas-temperature autocorrelation functions were computed and used to compute Lagrangian integral time scales. These scales are generally comparable to but larger than the Eulerian integral scales obtained from k-ε parameters as is typical for Lagrangian versus Eulerian scales. This latter point suggests the potential discontinuities associated with ODT triplet maps are not adversely affecting these statistics.
- Time-scales associated with rate of temperature change due to particles moving relative to the temperature field and changes due to diffusional mixing of the temperature field were characterized. The PDFs were peaked near zero with long tails suggesting strong intermittency. Since the rate of particle slip depends on the particle time constant, τ_p, the distribution of that rate of change associated with particle motion showed a strong dependence on τ_p. Diffusional temperature change, being independent of particle properties, did not exhibit this dependence. We took the logarithms of the absolute values for each of these rates and characterized the distributions of each; these distributions were more lognormal, and this might be a useful way to characterize these distributions.

References

[1] **A. R. Kerstein, "One-dimensional turbulence: Model formulation and application to homogenous turbulence, shear flows, and buoyant stratified flows," *J. Fluid Mech.,* vol. 392, pp. 277-334, 1999.**

[2] **A. R. Kerstein, W. T. Ashurst, S. Wunsch, and V. Nilsen, "One-dimensional turbulence: vector formulation and application to free shear flows," *J. Fluid Mech.,* vol. 447, pp. 85-109, 2001.**

[3] **W. T. Ashurst and A. R. Kerstein, "One-dimensional turbulence: Variable-density formulation and application to mixing layers," *Phys. Fluids,* vol. 17, p. 025107, 2005.**

[4] **R. Kumar, S. Saurav, E. V. Titov, D. A. Levin, R. F. Long, W. C. Neely, *et al.*, "Thermo-structural studies of spores subjected to high temperature gas environments," *Intl. J. Heat Mass Transfer,* vol. 54, pp. 755-765, Jan 31 2011.**

[5] **A. Y. Klimenko and R. W. Bilger, "Conditional Moment Closure for Turbulent Combustion," *Prog. Energy Combust. Sci.,* vol. 25, pp. 595-687, 1999.**

[6] **N. Peters, *Turbulent Combustion*: Cambridge University Press, 2000.**

[7] **J. R. Schmidt, J. O. L. Wendt, and A. R. Kerstein, "Prediction of particle laden turbulent channel flow using One-Dimensional Turbulence," in *IUTAM Symposium on Computational Approaches to Disperse Multiphase Flow*, Argonne, IL, 2004, pp. 433-441.**

[8] **G. Sun, D. O. Lignell, J. C. Hewson, and C. R. Gin, "Particle dispersion in homogeneous turbulence using the one-dimensional turbulence model," *Phys. Fluids,* vol. 26, p. 103301, 2014.**

[9] **D. O. Lignell, A. R. Kerstein, G. Sun, and E. I. Monson, "Mesh adaption for efficient multiscale implementation of one-dimensional turbulence," *Theoretical Comput. Fluid Dyn.,* vol. 27, pp. 273-295, Jun 2013.**

[10] **A. D. Gosman and E. Ioannides, "Aspects of computer simulation of liquid-fueled combustors," 1981.**

[11] **J. S. Shuen, L. D. Chen, and G. M. Faeth, "Evaluation of a stochastic model of particle dispersion in a turbulent round jet," *AIChE Journal,* vol. 29, pp. 167-70, 1983.**

[12] **J. C. Hewson, D. O. Lignell, and G. Sun, "Statistics of particle time-temperature histories: Progress report for August 2012," Sandia National Laboratories, SAND2012-73832012.**

[13] **J. R. Schmidt, J. O. L. Wendt, and A. R. Kerstein, "Non-equilibrium Wall Deposition of Inertial Particles in Turbulent Flow," *Journal of Statistical Physics,* vol. 137, pp. 233-257, Oct 2009.**

[14] **G. Sun, D. O. Lignell, and J. C. Hewson, "Stochastic simulation of Lagrangian particle transport in turbulent flows with two-way coupling," in preparation 2014.**

[15] **W. H. Snyder and J. L. Lumley, "Some measurements of particle velocity autocorrelation functions in a turbulent flow," *J. Fluid Mech.,* vol. 48, p. 41, 1971.**

[16] **M. R. Wells and D. E. Stock, "The effects of crossing trajectories on the dispersion of particles in a turbulent flow.," *J. Fluid Mech.,* vol. 136, pp. 31-62, 1983 1983.**

[17] **I. M. Kennedy and M. H. Moody, "Particle dispersion in a turblent round jet," *Exp. Therm. Flui. Sci,* vol. 18, pp. 11-26, 1998.**

[18] **S. G. Budilarto, "An experimental study on effects of fluid aerodynamics and particle size distribution in particle size distribution in particle-laden jet flows.," Purdue University, 2003.**

[19] **B. Y. H. Liu and J. K. Agarwal, "Experimental observation of aerosol deposition in turbulent flow," *Aerosol Science,* vol. 5, pp. 145-155, 1974.**

[20] **T. Zhu, R. Kumar, E. V. Titov, and D. A. Levin, "Analysis of Fractal-Like Spore Aggregates Using Direct Simulation Monte Carlo," *J. Thermophysics Heat Transfer,* vol. 26, pp. 417-429, Jul-Sep 2012.**

[21] **A. V. Filippov and D. E. Rosner, "Energy transfer between an aerosol particle and gas at high temperature ratios in the Knudsen transition regime," *Intl. Heat Mass Transfer,* vol. 43, pp. 127-138, Jan 2000.**

[22] **A. V. Filippov, M. Zurita, and D. E. Rosner, "Fractal-like aggregates: Relation between morphology and physical properties," *J. Colloid Interface Science,* vol. 229, pp. 261-273, Sep 1 2000.**

[23] **P. K. Yeung, "Lagrangian characteristics of turbulence and scalar transport in direct numerical simulations," *J. Fluid Mech.,* vol. 427, pp. 241-274, 2001.**

[24] **F. Toschi and E. Bodenschatz, "Lagrangian Properties of Particles in Turbulence," *Ann. Rev. Fluid Mech.,* vol. 41, pp. 375-404, 2009.**

Distribution (electronic)

1 Defense Threat Reduction Agency
Attn: Dr. S. Peiris
RD-BAS, Cube 3645E
8725 Kingman Road
Fort Belvoir, VA 22060-6201
Suhithi.Peiris@dtra.mil

1 Brigham Young University
Attn: Prof. David Lignell
350 Clyde Building
Provo, UT 84602
davidlignell@byu.edu

1	MS0815	Justine Johannes	1500
1	MS0836	John Hewson	1532
1	MS0836	Jeremy Lechmann	1516
1	MS1135	Randy Watkins	1532
1	MS1135	Allen Ricks	1532
1	MS1139	Dennis L. Miller	1530
1	MS1148	Josh Santarpia	6633
1	MS1148	Josh Hubbard	5754
1	MS9004	Duane Lindner	8100
1	MS0899	Technical Library	9536


Sandia National Laboratories